

TXS 0128+554: A Young Gamma-Ray Emitting AGN With Episodic Jet Activity

M. L. LISTER,¹ D. C. HOMAN,² Y. Y. KOVALEV,^{3,4,5} S. MANDAL,¹ A. B. PUSHKAREV,^{6,3} AND A. SIEMIGINOWSKA⁷

¹*Department of Physics and Astronomy, Purdue University, 525 Northwestern Avenue, West Lafayette, IN 47907, USA*

²*Department of Physics, Denison University, Granville, OH 43023, USA*

³*Astro Space Center of Lebedev Physical Institute, Profsoyuznaya 84/32, 117997 Moscow, Russia*

⁴*Moscow Institute of Physics and Technology, Institutskiy per. 9, Dolgoprudny 141700, Russia*

⁵*Max-Planck-Institut für Radioastronomie, Auf dem Hügel 69, 53121 Bonn, Germany*

⁶*Crimean Astrophysical Observatory, Nauchny 298688, Crimea, Russia*

⁷*Center for Astrophysics | Harvard and Smithsonian, 60 Garden St., Cambridge, MA 02138, USA*

(Received 30 April 2020; Revised 15 June 2020; Accepted 29 June 2020)

Submitted to *Astrophysical Journal*

ABSTRACT

We have carried out a *Chandra* X-ray and multi-frequency radio VLBA study of the AGN TXS 0128+554, which is associated with the *Fermi* γ -ray source 4FGL J0131.2+5547. The AGN is unresolved in a target 19.3 ks *Chandra* image, and its spectrum is well fit by a simple absorbed power law model, with no distinguishable spectral features. Its relatively soft X-ray spectrum compared to other CSOs may be indicative of a thermal emission component, for which we were able to obtain an upper temperature limit of $kT = 0.08$ keV. The compact radio morphology and measured advance speed of $0.32c \pm 0.07c$ indicate a kinematic age of only $82 \text{ y} \pm 17 \text{ y}$, placing TXS 0128+554 among the youngest members of the compact symmetric object (CSO) class. The lack of compact, inverted spectrum hotspots and an emission gap between the bright inner jet and outer radio lobe structure indicate that the jets have undergone episodic activity, and were re-launched a decade ago. The predicted γ -ray emission from the lobes, based on an inverse Compton-emitting cocoon model, is three orders of magnitude below the observed *Fermi* LAT flux. A comparison to other *Fermi*-detected and non-*Fermi* detected CSOs with redshift $z < 0.1$ indicates that the γ -ray emission likely originates in the inner jet/core region, and that nearby, recently launched AGN jets are primary candidates for detection by the *Fermi* LAT instrument.

1. INTRODUCTION

The *Fermi* LAT (4LAC) catalog of high-confidence AGN associations published by [The Fermi-LAT collaboration \(2019\)](#) contains 2863 γ -ray source detections above 0.1 GeV, 98% of which are classified as blazars or blazar candidates. These AGN have powerful relativistic jetted outflows aligned close to our line of sight, and dominate the γ -ray sky due to strong Doppler boosting of their high-energy emission (e.g., [Lister et al. 2009a](#); [Kovalev et al. 2009](#); [Savolainen et al. 2010](#)).

At present there are only a few known detections of weakly-boosted γ -ray emission from non-blazar (i.e.,

“misaligned”) AGN. Of the dozen γ -ray loud radio galaxies listed by [Rieger \(2016\)](#), all but 3 show either one-sided pc-scale jets and/or superluminal jet motion, indicative of small viewing angles. The exceptions are Centaurus A (distance $d = 4$ Mpc) and Fornax A ($d = 18$ Mpc), where resolved γ -ray emission has been detected from their kpc-scale lobes, and 3C 84 ($d = 70$ Mpc, in the Perseus cluster). The latter is unusual in terms of having two-sided radio jet structure on both pc- and kpc-scales, a strong compact radio core, and rapidly variable γ -ray emission ([Abdo et al. 2009](#)).

The *Fermi* catalog statistics suggest that extragalactic γ -ray emission can only be detected in either highly boosted jets, or in very nearby radio galaxies. However, there have been theoretical predictions of strong γ -ray emission from the pc-scale lobes of powerful young radio sources. These lobes are powered by

recently activated jets that are plowing into dense gas in their host galaxy (Stawarz et al. 2008; Kino et al. 2009, 2007; Kino & Asano 2011). Very few such candidates have been identified to date. Migliori et al. (2014) initially found no γ -ray counterparts at the locations of twelve young radio sources, but subsequently claimed a LAT detection near the position of PKS 1718–649 (Migliori et al. 2016). The latter is believed to have a kinematic age of less than 100 years (Giroletti & Polatidis 2009). Also McConville et al. (2011) and Müller et al. (2014) have claimed that the γ -ray AGN IERS B0954+556 and PMN J1603–4904, respectively, may either be young radio sources, or unusual examples of beamed blazars. Finally, Principe et al. (2020) have reported another young radio galaxy, NGC 3894, as a high-confidence LAT detection.

Here we present the results of a multi-frequency VLBA study of the nearby ($z = 0.0365$; Huchra et al. 2012) AGN TXS 0128+554, which is associated with the *Fermi* γ -ray catalog source 4FGL J0131.2+5547 / 3FHL J0131.1+5546. The radio source has a compact morphology that indicates it is a new example of a young, non-blazar AGN that is emitting at γ -ray energies. It is among the lowest luminosity γ -ray AGN detected by *Fermi* to date. We also present targeted 19 ks Chandra X-ray observations, and analyze the overall measurements in terms of the Stawarz et al. (2008) and Kino et al. (2009) cocoon models. We compare the physical characteristics of TXS 0128+554 to those of other known young AGN, and conclude that the *Fermi* LAT γ -ray detection of these radio sources depends strongly on both their cosmological distance and the current activity state of their inner jet region.

Throughout this paper we adopt the convention $S_\nu \propto \nu^\alpha$ for spectral index α , and use the cosmological parameters $\Omega_m = 0.27$, $\Omega_\Lambda = 0.73$ and $H_o = 71 \text{ km s}^{-1} \text{ Mpc}^{-1}$ (Komatsu et al. 2009). Under these assumptions the redshift of TXS 0128+554 corresponds to a luminosity distance of 158 Mpc and a linear scaling of 0.72 pc per milliarcsecond. With regards to the *Fermi* γ -ray observatory, we note that true *Fermi* AGN detections are rare, due to the poor angular localization of sources on the sky by the LAT instrument. They typically require additional information, such as co-temporaneous multi-wavelength variability. At the same time, the *Fermi* associations made on the basis of VLBI catalogs are shown to deliver a very low probability of chance coincidence (Kovalev 2009). For the purposes of this paper, we will refer to AGN listed as high-confidence associations in the *Fermi* LAT catalogs as *Fermi* detections.

2. BACKGROUND AND IDENTIFICATION

MOJAVE (Monitoring of Jets in AGN with VLBA Experiments) is a long term project to study the kinematic and polarization evolution of pc-scale AGN jets with regular VLBA imaging at 15 GHz (Lister et al. 2009b). It originally focused on a complete sample of the 135 strongest, most compact radio-loud AGN in the northern sky, and has been expanded during the *Fermi* era to encompass over 400 AGN. In September 2016, the survey added all AGN in the 3FGL catalog with mean γ -ray photon index harder than 2.1 and an associated radio source with at least 100 mJy of flux density at 15 GHz. The majority of these have a spectral energy distribution with a synchrotron peak above 10^{13} Hz, placing them in the intermediate- or high-spectral peaked classes. They are thus prime candidates for detection at TeV γ -ray energies with current (e.g., VERITAS, HESS, HAWC) and future high-energy observatories such as CTA.

The first VLBA images of these sources were obtained in late 2016, and show typical one-sided (core + jet) structures, similar to other AGN in the MOJAVE survey (Lister et al. 2018). However, the radio galaxy TXS 0128+554 stood out as having a two-sided (lobe-core-lobe) morphology similar to known compact symmetric objects (CSOs). This class was first identified in the 1990s and generally consists of young radio sources that enter into flux-density-limited surveys due to their powerful pc-scale lobe emission (O’Dea 1998). Because they are not selected on the basis of Doppler boosted jet emission, they are not subject to orientation bias, and therefore are more likely have jets lying close to the plane of the sky. Their lobe emission is usually confined to pc-scales, and typically dominates over that of the core, resulting in either a convex spectrum, or one that remains steep down to MHz frequencies. The radio emission from GPS/CSO jets is often strongly depolarized due to dense ionized gas in their external environment (Aller et al. 2003; Dallacasa et al. 2013; Tremblay et al. 2016).

The radio source TXS 0128+554 is positionally coincident with the nucleus of a $K_s = 10.7$ mag elliptical galaxy in the 2MASS survey at $z = 0.036$ (158 Mpc; Huchra et al. 2012). Its WISE infrared colors place it within the blazar color-color strip as defined by Masaro et al. (2012) but well outside the region occupied by γ -ray-loud blazars. It is associated with the *ROSAT* X-ray source RX J0131.2+5545, and the LAT source 4FGL J0131.2+5547. The radio position is offset 116 arcsec from the LAT centroid, but is within the 95% confidence ellipsoid dimensions of 143 arcsec by 122 arcsec. The γ -ray source was listed in the *Fermi* 3LAC (high-confidence AGN) catalog (Ackermann et al. 2015)

Table 1. VLBA Image Properties

ν (GHz)	I_{tot} (mJy)	I_{peak} (mJy bm^{-1})	Maj. (mas)	Min. (mas)	PA ($^{\circ}$)	I_{rms} (mJy bm^{-1})	I_{base} (mJy bm^{-1})
(1)	(2)	(3)	(4)	(5)	(6)	(7)	(8)
2.3	207	79	5.71	4.42	-10.2	0.07	0.30
5	162	61	2.21	1.87	0.3	0.03	0.10
6.6	151	62	1.63	1.37	-3.1	0.04	0.15
8.4	151	64	1.35	1.12	-9.0	0.05	0.16
15.4	114	63	0.70	0.58	-11.8	0.04	0.12
22.2	97	84	0.53	0.45	-8.8	0.06	0.20

NOTE—Columns are as follows: (1) observing frequency (GHz), (2) total cleaned flux density (mJy), (3) map peak (mJy per beam), (4) FWHM major axis of restoring beam (milliarcseconds), (5) FWHM minor axis of restoring beam (milliarcseconds), (6) position angle of major axis of restoring beam (degrees), (7) rms noise level of image (mJy per beam), (11) lowest I contour (mJy per beam).

but not in 4LAC (The Fermi-LAT collaboration 2019). In the 4FGL catalog it is fitted by a single power law spectrum of index = 2.10 ± 0.09 and an energy flux of 5.6×10^{-13} erg cm^{-2} s^{-1} between 0.1 GeV and 100 GeV (detection significance = 11 sigma). It has a γ -ray variability index of 62, which is below the value of 72 at which sources in the 4FGL are considered variable at > 99% confidence (Abdollahi et al. 2020). Its properties above 10 GeV are also tabulated in the 3FHL catalog (Ajello et al. 2017), with a relatively steep power law index of 3.1 ± 0.9 and no significant spectral curvature. The source was listed as an association with 3FGL J0131.3+5548 in the 3FGL catalog (Acero et al. 2015), which included *Fermi* data from 2008–2012, but not in any of the previous EGRET or *Fermi* γ -ray catalogs. No observations have been reported to date at TeV energies.

3. OBSERVATIONAL DATA

3.1. Multi-frequency VLBA observations

We observed TXS 0128+554 over a 13 h period on 2018 June 29 (obscode BL251) with the VLBA. The North Liberty antenna did not participate due to a damaged elevation motor. Two scans were made of the bright radio blazar TXS 0059+581 for fringe calibration. During each of the target and calibrator pointings, scans were made successively at central observing frequencies of 2.3 GHz, 5.0 GHz, 6.6 GHz, 8.4 GHz, 15.4 GHz, 22.2 GHz. The data were recorded at 2048 Mbps in dual circular polarization, with a bandwidth of 256 MHz at each frequency.

We processed the data in AIPS (Greisen 2003) following standard procedures, and self-calibrated and imaged

the data with the Difmap package (Shepherd 1997). Approximately 40% of the data at 2.3 GHz were unusable due to radio frequency interference from satellite radio signals. In Figure 1 we show the natural-weight total intensity contour maps at all six frequencies, and list the map properties in Table 1.

We fitted bright jet features in the visibility plane to the 15 GHz data and other MOJAVE 15 GHz epochs (§ 4.3) with circular Gaussians (Table 2). Based on previous analysis (Lister et al. 2009c), the typical uncertainties in the feature centroid positions are $\sim 20\%$ of the FWHM naturally-weighted image restoring beam dimensions. For the bright and compact features, the positional errors are smaller by approximately a factor of two. We estimate the formal errors on the feature sizes to be roughly twice the positional error, according to Fomalont (1999). The flux density accuracies are approximately 5% (Homan et al. 2002).

3.2. X-ray Observations

The *Chandra* ACIS-S (Weisskopf et al. 2002) observations of TXS 0128+554 were performed in four separate pointings during March–April 2019 (see Table 3 for details). The source was placed at the default aim point on the back-illuminated ACIS charge coupled device (CCD, ACIS-S3). The VFaint mode and 1/8 CCD readout mode was used to avoid a potential pile-up (see *Chandra* Proposer Observatory Guide¹). The source was detected in each individual observation, resulting in a total exposure time of 19.3 ks.

¹ see <https://cxc.harvard.edu/proposer/POG/>

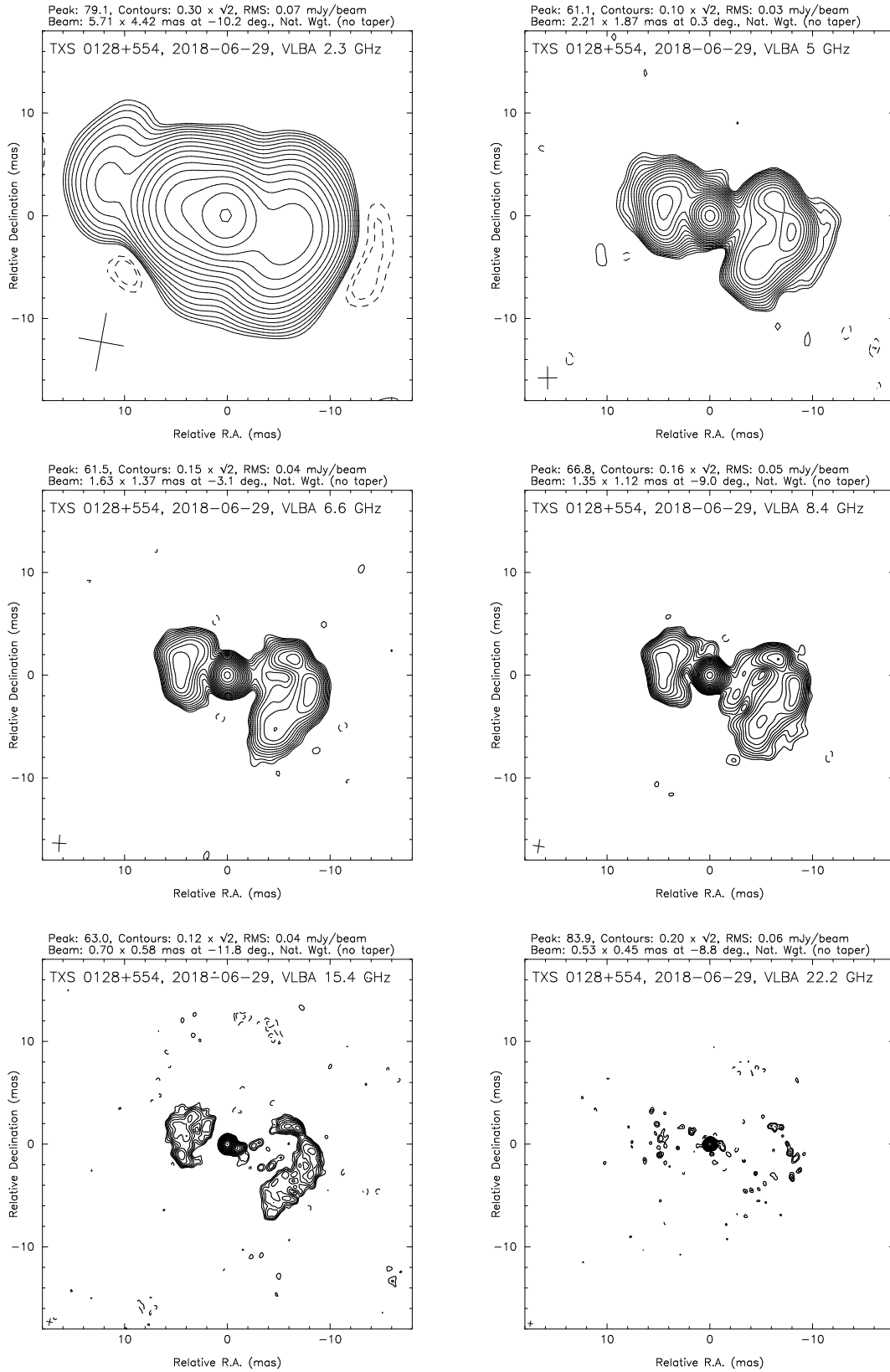


Figure 1. Clockwise from the top left: total intensity VLBA contour maps of TXS 0128+554 at 2.3 GHz, 5 GHz, 6.6 GHz, 8.4 GHz, 15.4 GHz, and 22.2 GHz. The Gaussian FWHM restoring beam dimensions of each map are indicated by a cross in the lower left corner of each panel.

Table 2. Fitted 15 GHz Jet Features

I.D.	Epoch	I (mJy)	r (mas)	P.A. ($^{\circ}$)	Maj. (mas)	log T_b (K)
(1)	(2)	(3)	(4)	(5)	(6)	(7)
C0	2016 Sep 26	59.2	0.02	199.0	0.15	10.1
C0	2016 Nov 6	56.4	0.15	10.1
C0	2016 Dec 10	54.1	0.11	10.4
C0	2017 Jan 28	51.9	0.14	10.1
C0	2017 Jul 30	56.8	0.12	10.3
C0	2017 Nov 18	63.3	0.16	10.1
C0	2018 Jun 29	49.7	0.04	91.0
C0	2019 Aug 23	41.9	0.02	101.3	0.09	10.4
C1	2016 Sep 26	2.5	4.59	105.5	0.49	7.7
C1	2016 Nov 6	3.0	4.62	105.0	0.64	7.6
C1	2016 Dec 10	2.4	4.64	103.6	0.55	7.6
C1	2017 Jan 28	2.5	4.64	104.1	0.50	7.7
C1	2017 Jul 30	1.5	4.58	102.5
C1	2017 Nov 18	3.1	4.51	104.0	0.87	7.3
C1	2018 Jun 29	3.7	4.52	104.2	0.96	7.3
C1	2019 Aug 23	4.2	4.45	104.6	1.43	7.0

NOTE—Columns are as follows: (1) feature identification number (zero indicates core feature), (2) observation epoch, (3) flux density at 15 GHz in mJy, (4) position offset from the core feature (or map center for the core feature entries) in milliarcseconds, (5) position angle with respect to the core feature (or map center for the core feature entries) in degrees, (6) FWHM major axis of fitted Gaussian in milliarcseconds, (7) log of brightness temperature in Kelvin. (This table is available in its entirety in machine-readable form.)

Table 3. Chandra Observations

Date	OBSID	Exposure (ks)	Net Counts ^a
2019 Mar 29	21408	5.76	400.4 \pm 20.6
2019 Mar 30	22160	6.68	528.2 \pm 23.1
2019 Mar 31	22161	3.84	301.5 \pm 17.0
2019 Apr 01	22162	3.06	257.9 \pm 16.1

^a Net counts given for a circular source region with a radius $r = 1.5$ arcsec, with 1σ errors.

We performed the X-ray analysis of the *Chandra* observations with CIAO software version 4.12 (Fruscione et al. 2006) and the *Chandra* calibration data base version 4.9. We reprocessed the pipeline data by running the `chandra_repro` CIAO tool in order to apply the ver-

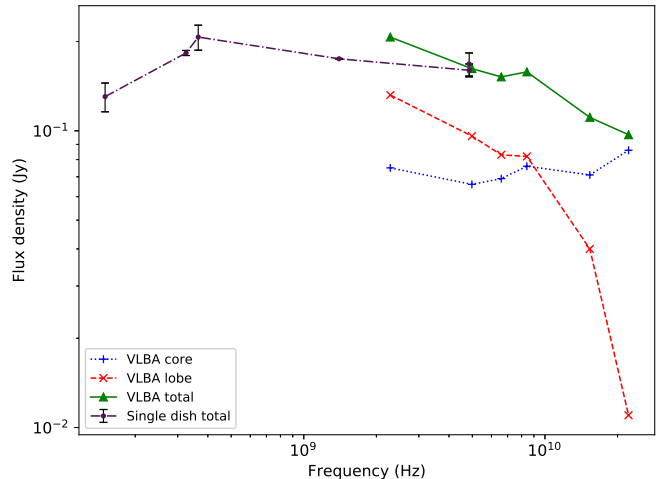


Figure 2. Continuum radio spectrum plot for TXS 0128+554. The single dish flux densities (purple dot-dashed curve) are taken from published surveys as listed in NED. The solid green curve represents total VLBA flux density measurements from our observations, while the red dashed and blue dotted curves represent the pc-scale lobe and core components, respectively.

sion 4.9 of the ACIS-S calibration, and used the sub-pixel event repositioning algorithm² (`pix_adj=EDSER`) to obtain the highest resolution X-ray image.

We performed the initial inspection of the data in `ds9` (Joye & Mandel 2003) displaying the event files and confirming a strong detection of the source in each individual observation. We defined the source region to be a circle with the 1.5 arcsec radius corresponding to $\sim 95\%$ fraction of the *Chandra* point spread function, PSF) centered at the source position J2000(RA,Dec) = (01:31:13.8,+55:45:13.2). We assumed a background region to be an annulus centered on the source position with the radii between 2.5 arcsec and 4.5 arcsec. We discuss the details of the X-ray spectral fitting analysis in Section 4.5.

4. DATA ANALYSIS

4.1. Radio morphology

The radio source TXS 0128+554 is unresolved in the 1.4 GHz NVSS (Condon et al. 1998), GMRT (Intema et al. 2017), and 2–4 GHz VLASS (Lacy et al. 2020) sky surveys, and in a 5 GHz VLA snapshot image taken in 1994 (Laurent-Muehleisen et al. 1997). The overall radio spectrum is peaked below 1 GHz (§ 2), with no upturn at low-frequencies that might be expected if significant steep-spectrum extended lobe emission were present.

² <https://cxc.harvard.edu/ciao/why/acissubpix.html>

The pc-scale radio morphology of TXS 0128+554 (Figure 1) consists of a bright unresolved core feature flanked by two arc-shaped radio lobes. This is typical of the compact symmetric object class of young radio sources (Wilkinson et al. 1994). The leading edges of the lobes appear brightened, indicative of interaction with the host galaxy’s interstellar medium. The radio structure is similar to the two-sided inner lobe morphology of the radio galaxy 3C 84 (NGC 1275; $d = 70$ Mpc), which has a similar overall diameter (~ 9 pc) and has been modeled as an expanding plasma cocoon by Fujita et al. (2016).

The overall projected extent of the lobes is similar in the images at 6.6 GHz and at higher frequencies, ranging from 3.2 pc to 4.3 pc from the core for the eastern lobe, and from 4.5 pc to 6.5 pc for the western lobe. The 2.3 and 5 GHz images reveal faint steep-spectrum emission regions farther out, at 8.8 pc (eastern lobe), and at 7.8 pc (western lobe) from the core, respectively. These steep-spectrum regions are aligned along the source axis at 256° that is defined by the position angles of features C2 and C6, and the bright inner jet features C8, C9, and C10 (see Fig. 3 and Table 2).

4.2. Spectral index map and the core-shift effect

We created a spectral index map from the 5 GHz – 22.2 GHz data by aligning the maps on the core feature positions. We checked for possible opacity-related core shifts (e.g., Sokolovsky et al. 2011; Pushkarev et al. 2012; Voitsik et al. 2018) by applying small shifts in different directions and calculating the standard deviation of the spectral index values for all pixels within 1.5 beamwidths of the core position. For all of the frequency maps the minimum standard deviation value occurred for shifts smaller than 0.03 mas, so we chose to not apply any shifts before combining the final maps. A similar approach was used and proven to be efficient and robust by Plavin et al. (2019).

We also checked the results of the alignment using an alternative approach to estimate the core shift effect. The algorithm is based on the fast normalized cross-correlation (Lewis 1995) to register the total intensity maps at different frequencies assuming no strong spectral gradients within the matched areas. We first convolved all the maps with the same circular beam size 1.4 mas and a small pixel size of 0.06 mas, which corresponds to the positional accuracy of the core feature. We then performed the image registration using the optically thin regions of western lobe. We detected no shift for any of the frequency pairs, confirming our other result that was based on minimizing the standard deviation of the spectral index.

To construct the spectral index map we applied a Gaussian taper to the maps above 8 GHz, and restored each map with a circular beam of $\text{FWHM} = 1.4$ mas and a pixel size of 0.3 mas. The former corresponds to the minimum dimension of the uniformly weighted 5 GHz restoring beam. We blanked any pixels with intensity below three times the noise level at any frequency, and calculated the spectral index for the remaining pixels using single power law fits. We note that at the highest frequencies, there is sparser coverage at short spacings in the (u, v) plane, which can result in less sensitivity to diffuse lobe emission and some artificial steepening of the spectra.

In Figure 3 we show the spectral index map in false color, superimposed on the 5 GHz total intensity contours. The map reveals an inverted spectrum core region with $\alpha \simeq +0.2$, which steepens to $\alpha \simeq -0.5$ at $r = 2$ mas west of the core. The lobe regions have spectral indices in the range $-0.7 < \alpha < -1.1$. The two steepest spectrum regions in the lobes are located on the source axis, slightly further from the core than features C2 and C6.

Although TXS 0128+554 displays a flat-spectrum core region typically seen in compact jetted AGN, its negligible core shift is unusual. For a typical AGN jet with dominating synchrotron opacity and seen at small viewing angle, one would expect a core shift between 5 and 22 GHz to be about 0.3 mas (e.g., Pushkarev et al. 2012). This is an order of magnitude larger than our upper limit that corresponds to a projected distance of 0.02 pc. It could result from not being able to separately resolve the emission from the approaching and receding jets very close to the core, but we note that there are other high viewing angle AGN jets with measurable core shifts (e.g., NGC 4261; Haga et al. 2015 and NGC 315; Pashchenko & Plavin 2019).

Alternatively, we propose that the nature of the apparent radio core in TXS 0128+554 is not the optically thick $\tau = 1$ surface, but rather a recollimation or reconfinement shock (e.g., Cohen et al. 2014; Fromm et al. 2013; Kovalev et al. 2020), the position of which is not frequency dependent. We note that the inverted spectral index value of $\sim +0.2$ in the core region further supports this scenario. The latter could be a result of absorption by a circumnuclear torus, but additional VLBI spectral line studies would be needed to further investigate this possibility.

4.3. Multi-epoch VLBA data and jet kinematics

TXS 0128+554 was added to the MOJAVE VLBA monitoring program (Lister et al. 2019) in 2016 after its detection as a hard-spectrum (3FHL catalog photon

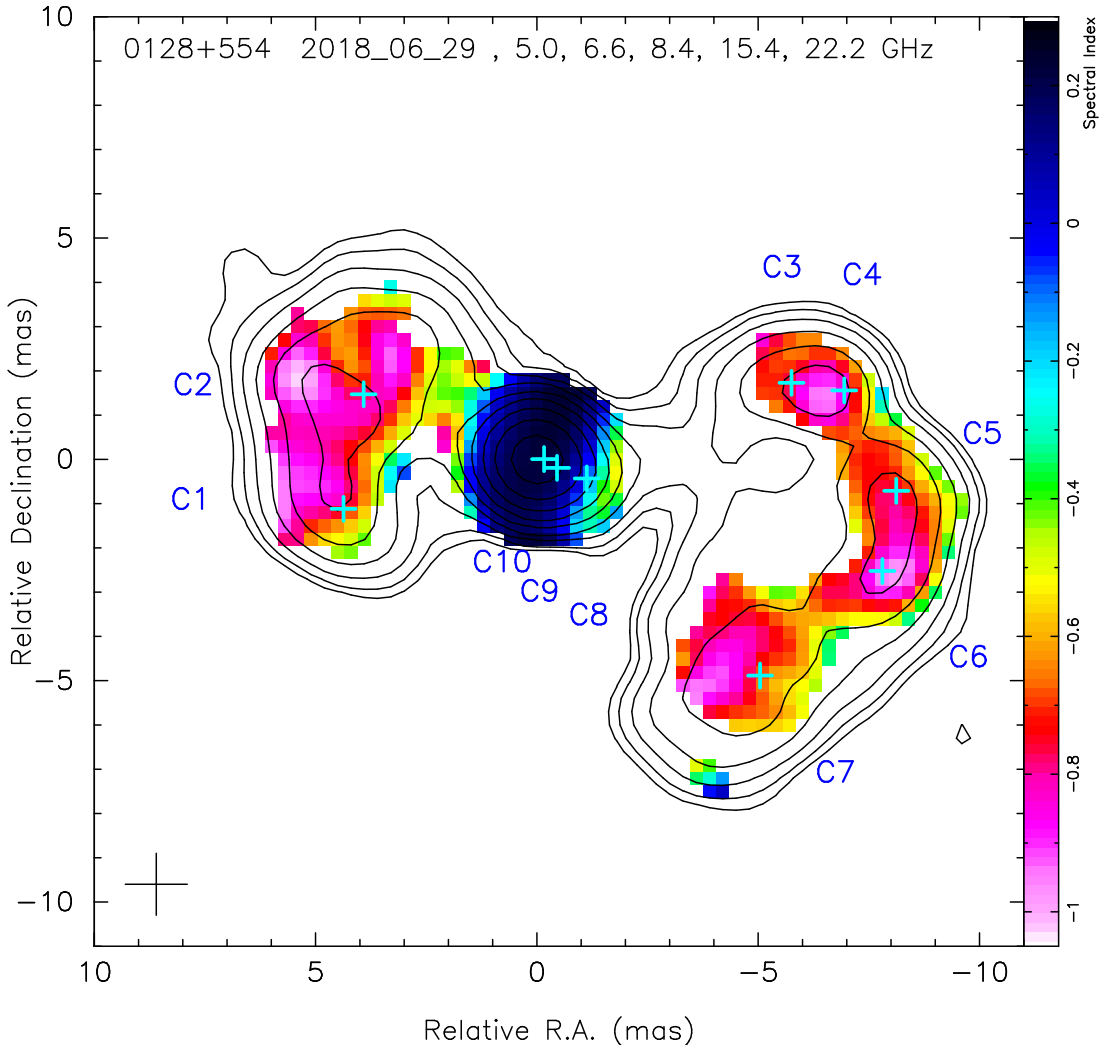


Figure 3. Total intensity 5 GHz contour map of TXS 0128+554, with spectral index map superimposed in false color. The crosses indicate the Gaussian feature positions fitted to the 15 GHz 2018 June 29 epoch. The spectral indices are derived from a single power-law fit to the pixel values at 5 GHz, 6.6 GHz, 8.4 GHz, 15.4 GHz, and 22.2 GHz. We aligned the individual frequency maps on the core feature C0 (position at the origin) and restored them with a common circular beam of FWHM = 1.4 mas and a pixel size of 0.3 mas.

index $\Gamma = 2.1$) γ -ray source by the *Fermi* LAT instrument (Ajello et al. 2017). We obtained a total of seven VLBA 15 GHz epochs between 2016 September 26 and 2019 August 23. In Figure 4 we show a stacked total intensity image of these epochs (plus the 2018 June 29 BL251 non-MOJAVE epoch), restored with a circular beam of FWHM = 0.5 mas and pixel size of 0.1 mas. The MOJAVE observations were also sensitive to linear polarization, but we detected no significant polarized flux density at any epoch, with upper limits on the fractional polarization of 0.5%.

We fitted the interferometric visibilities at each 15 GHz epoch using Gaussian features as in Lister et al. (2019) and list their properties in Table 2. The outer jet features (C1 – C7) display very little flux density variability, and are weak and diffuse, with brightness tem-

peratures (T_b) between 10^6 K and 10^8 K. The innermost jet features (C8 – C10) vary in flux density by a factor of 2–3 over the epochs and are more compact, with T_b values between 10^8 K and 10^9 K. The core feature maintains a steady brightness temperature of $\sim 10^{10}$ K but shows a drop in flux density by roughly 30% between 2017 November and 2019 August. The core T_b is one to two orders of magnitude lower than typical blazars in the MOJAVE program (Lister et al. 2011), and is similar to those of less Doppler-boosted radio galaxies and members of the CSO/GPS class (Nagar et al. 2005). Stable radio flux densities are a common characteristic of the CSO/GPS class, since their jet emission is less affected by relativistic Doppler boosting (Fassnacht & Taylor 2001). We fit the Gaussian component positions with respect to the (presumed stationary) core feature at

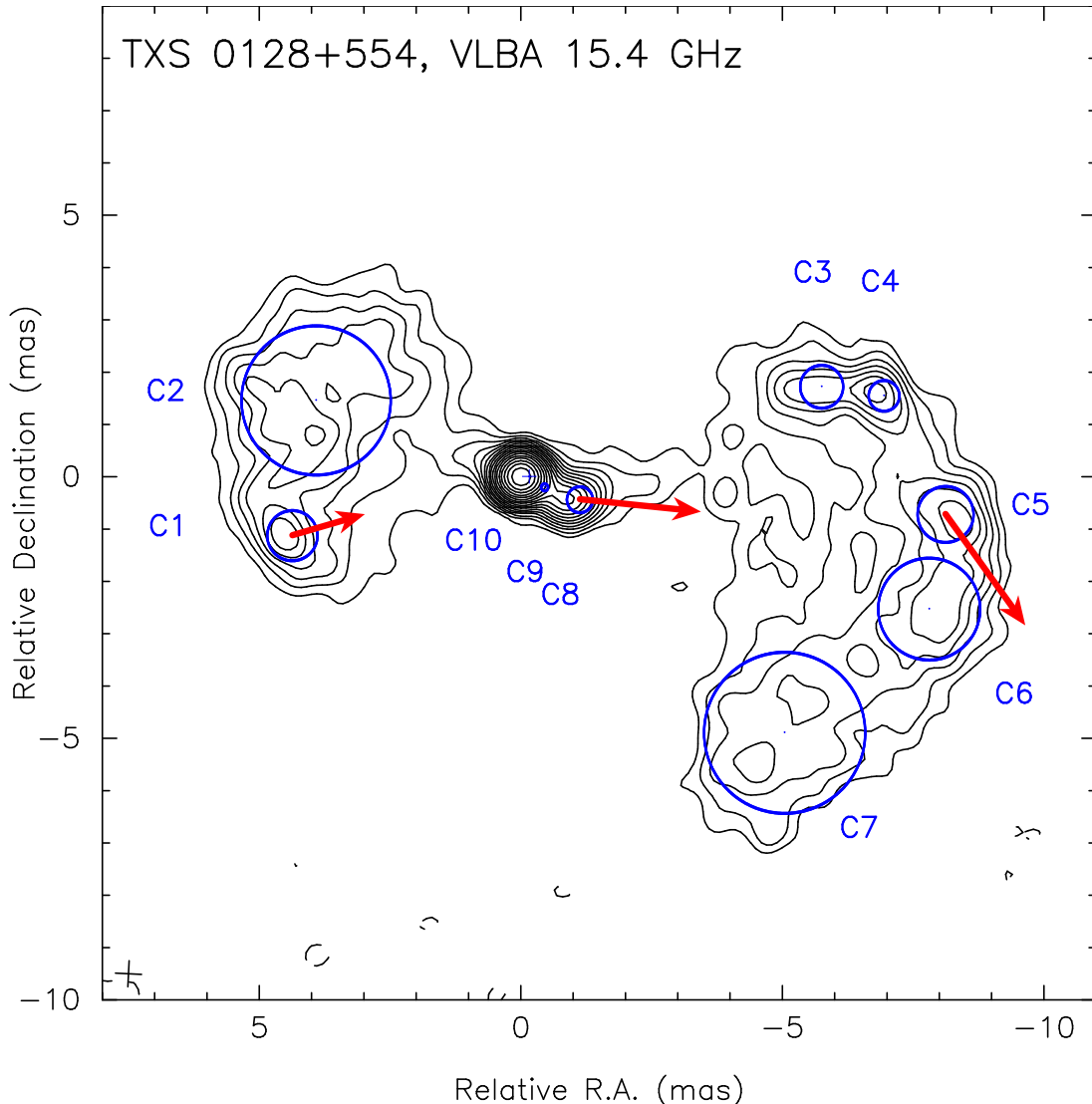


Figure 4. Stacked epoch 15 GHz VLBA contour image of TXS 0128+554, which combines 8 epochs between 2016 September 26 and 2019 August 23, aligned on the core feature C0 (positioned at the origin) and restored with a circular beam of FWHM = 0.5 mas. The contours are $\sqrt{2}$ times the base contour level of 0.15 mJy per beam. The blue circles indicate the FWHM Gaussian diameters of features fit to the 2018 June 29 epoch at 15 GHz, and the red arrows are representative of their fitted proper motion vectors. Their lengths correspond to the projected displacement in 20 years assuming constant speed. Only features C1, C8 and C5 have significant proper motion.

each 15 GHz epoch with a simple vector motion model, as described in [Lister et al. \(2019\)](#). Our code fits a constant velocity independently in the right ascension and declination directions, and solves for the feature position at a reference epoch date (2018.19) that is midway between the first and last epoch. We list the kinematic fit parameters for each feature in Table 4.

Most of the features display no significant proper motion over the ~ 3 year monitoring period, with the exception of C1, C5 and C8. The inner features C9 and C10 do not have sufficient epochs for a reliable proper motion determination, and any apparent motion

of the off-axis features may be affected by the three-dimensional expansion of the lobes. The velocity vector directions of C5 and C8 do not point back to the direction of the core feature, indicating a current or past acceleration (Fig. 4). Also, the separation of C1 and the core is decreasing at a rate of $72 \pm 18 \mu\text{as y}^{-1}$, which may be due to projection effects, backflow of plasma from the lobe, or changes in the feature’s internal brightness distribution. A comparison of the 2019 June epoch at 8 GHz with an archival 2010 August epoch (VLBA obscode = BC191I, PI = Jim Condon) shows an outward shift of $127 \mu\text{as y}^{-1}$ of C5 along PA = 209° , which is

Table 4. Vector Motion Fit Properties of Jet Features

I.D.	$\langle S \rangle$ (mJy)	$\langle R \rangle$ (mas)	$\langle d_{\text{proj}} \rangle$ (pc)	$\langle \vartheta \rangle$ (deg)	ϕ (deg)	$ \langle \vartheta \rangle - \phi $ (deg)	μ ($\mu\text{as y}^{-1}$)	β_{app} (c)	α_m (μas)	δ_m (μas)
(1)	(2)	(3)	(4)	(5)	(6)	(7)	(8)	(9)	(10)	(11)
C1	3	4.58	3.28	104.2	286 ± 20^a	178 ± 20	72 ± 18	0.174 ± 0.042	4408 ± 18	-1111 ± 28
C2	15	4.16	2.98	71.3	40 ± 34	31 ± 34	59 ± 31	0.143 ± 0.075	3963 ± 19	1355 ± 42
C4	4	6.99	5.00	283.3	257 ± 28	26 ± 28	80 ± 31	0.193 ± 0.076	-6847 ± 33	1598 ± 41
C5	5	8.16	5.84	265.1	216 ± 13	50 ± 13^b	131 ± 30	0.317 ± 0.072	-8168 ± 26	-750 ± 35
C6	6	8.26	5.91	252.4	225 ± 40	28 ± 39	87 ± 51	0.21 ± 0.12	-7910 ± 61	-2534 ± 51
C7	9	6.88	4.92	227.5	63 ± 85	164 ± 85	38 ± 67	0.09 ± 0.16	-5048 ± 74	-4639 ± 72
C8	6	1.01	0.72	245.7	264.1 ± 4.7	18.4 ± 4.7^b	116 ± 25	0.282 ± 0.062	-980 ± 27	-420.8 ± 9.0

^aFeature has significant inward motion.

^bFeature has significant non-radial motion.

NOTE—Columns are as follows: (1) feature number, (2) mean flux density at 15 GHz in mJy, (3) mean distance from core feature in mas, (4) mean projected distance from core feature in pc, (5) mean position angle with respect to the core feature in degrees, (6) position angle of velocity vector in degrees, (7) offset between mean position angle and velocity vector position angle in degrees, (8) proper motion in $\mu\text{as y}^{-1}$, (9) apparent speed in units of the speed of light, (10) fitted right ascension position with respect to the core at the middle epoch (2018.19) in μas , (11) fitted declination position with respect to the core at the middle epoch (2018.19) in μas .

consistent with the C5 speed measurement at 15 GHz from 2016–2019.

The apparent speeds of C5 ($0.32 c \pm 0.07 c$) and C8 ($0.28 c \pm 0.06 c$) are self-consistent to within the errors, and are similar to the sub-luminal expansion speeds measured in other GPS/CSO jets (Gugliucci et al. 2005). Given the double-lobed morphology of this source, its jets likely lie close to the plane of the sky (see § 4.4), and superluminal motion is therefore not expected.

4.4. Intrinsic jet speed and viewing angle

The asymmetry of the jet morphology and reasonably high apparent velocities of features C5 and C8 suggest that the radio properties of TXS 0128+554 are affected by relativistic beaming and time delay effects. In this case, the western (approaching) jet and lobe emission are Doppler boosted, while the eastern lobe emission is de-boosted. The eastern lobe emission also has to travel a longer distance to the observer, so we are seeing it at an earlier stage of its evolution (and thus with a smaller apparent size). In the same vein, the photons we see from the western lobe were emitted at a later stage of the sources' evolution than those from the core region.

Under the assumption of identical jet and counter-jet expansion speeds $v = \beta c$ at viewing angles θ and $180^\circ - \theta$ from the line of sight, respectively, we can use the apparent separation of two jet features located on opposite sides of the core to measure $\beta \cos \theta$ (Ryle &

Longair 1967). Considering only time-lag effects, the expected separation ratio is

$$Q = \frac{1 + \beta \cos \theta}{1 - \beta \cos \theta}.$$

Because the location of C2 represents the centroid of a complex emission region, we use the two steepest spectrum locations in the lobes, at $r = 5.6 \pm 0.1$ mas and $r = 8.4 \pm 0.1$ mas along the main jet axis (PA = 256°). This yields $Q = 1.50 \pm 0.03$ and $\beta \cos \theta = 0.20 \pm 0.01$. The separation ratio for the mean positions of features C4 and C1 (Table 4) yields a similar value of $Q = 1.53 \pm 0.03$, which would be expected if the lobes are expanding radially from the central source.

The expected flux density ratio due to relativistic boosting is

$$J = \left[\frac{1 + \beta \cos \theta}{1 - \beta \cos \theta} \right]^p.$$

The boosting index p is $2 - \alpha$ for continuous jet emission, and $3 - \alpha$ for an isolated bright feature, where α is the spectral index (Urry & Padovani 1995).

There are several possible ways to measure J in the source. The first is to sum the emission from each lobe, excluding the core feature, which gives $J = (42 \pm 2 \text{ mJy}) / (21 \pm 1 \text{ mJy}) = 2.0 \pm 0.1$. A second method involves taking a slice along the main jet axis in the 15 GHz stacked epoch image. There is an initial peak of $J = 5.5 \pm 0.5$ at the location of feature C8, where

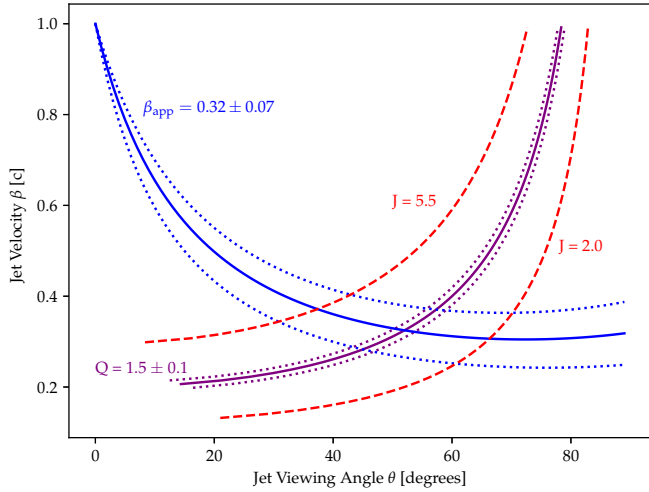


Figure 5. Diagram showing constraints on jet speed β and viewing angle θ derived from the apparent jet speed (blue solid curve), jet/counter-jet length ratio (purple solid curve) and jet/counter-jet flux density ratios (red dashed curves). The dotted curves represent the $\pm 1\sigma$ ranges on the measured quantities. The intersection point of the β_{app} and Q curves is at $\theta = 52^\circ$, $\beta = 0.32$.

$\alpha = -0.07 \pm 0.04$. J drops below unity until $r = 6.2$ mas, and then rises to a plateau of $J = 1.8 \pm 0.1$ at $r = 6.5$ mas. Past $r \gtrsim 7$ mas, J rapidly rises above 8 due to the smaller size of the eastern lobe.

The interpretation of the jet/counter-jet flux density ratio is complicated by the time delay effects in the two lobes. For example, if feature C8 represents a (more recent) large jet outburst, its counterpart feature in the eastern jet may be located very close to the core and not currently resolvable in the 15 GHz image. Likewise, the total flux density of each lobe represents emission at different evolutionary stages and thus may not be intrinsically identical.

In Figure 5 we plot the constraints on $\beta \cos \theta$ based on the measured apparent speed, separation ratio, and flux density ratio. For the latter, we assume $p = 2.8$ and plot two dashed curves, for $J = 2.0$ and $J = 5.5$. The dotted curves represent the $\pm 1\sigma$ ranges. The measured quantities constrain the intrinsic jet velocity to the range $0.25 < \beta < 0.4$. The apparent speed and jet length ratio provide a narrower constraint on the viewing angle ($43^\circ < \theta < 59^\circ$) than the flux density ratios ($31^\circ < \theta < 70^\circ$). The intersection point of the β_{app} and Q curves is at $\theta = 52^\circ$, $\beta = 0.32$, which corresponds to mild Doppler boosting factors of $\delta = 1.2$ in the approaching jet and $\delta = 0.79$ in the counter-jet.

By assuming that the plasma in the western lobe has been expanding at constant velocity of $0.32 c$ and using its de-projected size, we derive a kinematic age of $r_{\text{max}}/c\beta_{\text{app}} = 82 \pm 17$ years. This places TXS 0128+554

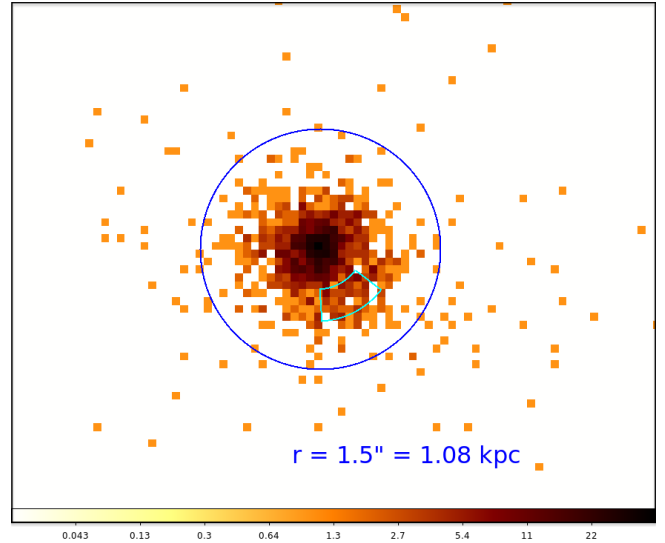


Figure 6. The *Chandra* ACIS-S X-ray image centered on TXS 0128+554 (image size $7.5'' \times 6.2''$). The four individual observations have been merged. The image is binned to $0.246''$, half of the native ACIS pixel size. The circle marks the region assumed for the spectral extraction (radius of $1.5'' = 1.08$ kpc) and containing 95% fraction of the PSF counts. The *Chandra* PSF artifact region is marked with the cyan color. The color intensity represents the number of counts per pixel with the color bar showing the scale.

among the youngest known relativistic AGN jet systems. We compare its properties to other recently launched AGN jets in Section 5.3.

4.5. *Chandra* X-ray Analysis

The *Chandra* ACIS-S observations of TXS 0128+554 were taken at four separate epochs and needed to be merged into one event file for detailed image analysis of the spatial properties of the source, and to look for any extended structures. We merged individual *Chandra* observations using `reproject_obs` in CIAO. For each observation we simulated the *Chandra* point spread function (PSF) using `simulate_psf`, and merged the individual simulations into one image file. We then used both images to generate the radial surface brightness profiles of the source and the PSF, assuming a set of annuli centered at the (J2000) coordinates: RA=1:31:13.8588, DEC=+55:45:13.532. We excluded the position angle covered by the known PSF asymmetry region given by `make_psf_asymmetry_region`. The final radial profiles were fit to check for any extended features and were found to be consistent with a point source. We show the merged *Chandra* image centered on TXS 0128+554 in Fig. 6.

We extracted the spectra and all the corresponding standard calibration files (i.e., `arf` and `rmf`) for each

observation using `specextract` in CIAO³, assuming the source and background regions defined above. We performed all spectral modeling of the *Chandra* X-ray data in *Sherpa*⁴ (Freeman et al. 2001; Refsdal et al. 2009). We used Cash and Cstat fitting statistics (Cash 1979) and the Nelder-Mead optimization method (Nelder & Mead 1965). We tabulate the fit parameters resulting from a simultaneous fit of all spectra in Table 5. The fitted total X-ray luminosities are 3.2×10^{42} erg s⁻¹ between 0.5 keV and 2 keV, and 2.1×10^{42} erg s⁻¹ between 2 keV and 10 keV.

In all models we assumed a constant Galactic absorption column of 2.6×10^{20} cm⁻² (from COLDEN⁵, Stark et al. 1992). We initially fit an absorbed power law model and obtained the best fit photon index, $\Gamma = 2.38 \pm 0.10$ and an intrinsic absorber at $z = 0.0365$ with an equivalent column of hydrogen of $N_H(z) = 6.7 \times 10^{21}$ cm⁻². The latter is in agreement with the H absorbing column density of 1.2×10^{21} cm⁻² predicted from the N_{H_I} – linear size relation found by Pihlström et al. (2003).

Recent studies of neutral N_{H_I} (21 cm) and total N_H (X-rays) absorbing columns in compact radio AGN indicate a correlation between the two column densities, with a scatter related to the spin temperature and a covering fraction of the absorbing gas (Ostorero et al. 2010, 2017). Our X-ray measurement of $N_H(z)$ and the extrapolated N_{H_I} value place TXS 0128+544 at the upper part of this scatter, indicating a larger amount of neutral medium in comparison to the sources with similar N_H . A future detection of 21 cm absorption could provide an important data point for this correlation. Interestingly, the TXS 0128+544 X-ray absorption is in agreement with the relation between the radio source size, radio luminosity and a total N_H column studied by Sobolewska et al. (2019), in which the more compact CSOs show higher absorption columns. However, these correlation results were based on a small number of CSOs observed in X-rays and they require confirmation with larger samples.

The photon index of $\Gamma = 2.38$ is steep in comparison to a more typical value of $\Gamma_{\text{ave}} \sim 1.7$ found in other CSOs with *Chandra* spectra (Siemiginowska et al. 2016). The soft X-ray spectrum might be due to a hot thermal gas in the central kpc-scale region. We therefore added a thermal component to the spectral model and obtained an upper limit on the temperature of $kT = 0.08$ keV

(APEC⁶ model in *Sherpa*). The contribution from such thermal emission would dominate the spectrum at lower energies. However, the current *Chandra* spectra do not provide any constraint on the fraction of thermal radiation within the nuclear, < 1 kpc region, and no diffuse X-ray hot gas outside that region above the background flux level of 2.6×10^{-15} erg s⁻¹ cm⁻².

We also looked for an iron line at 6.4 keV often indicating a presence of a reflection of the primary absorbed X-ray radiation off the cold medium (e.g., a large scale clumpy torus; see Hickox & Alexander 2018 for a review). We fit the spectrum with an absorbed power law model (fixed $N_H(z) = 7 \times 10^{21}$ cm⁻²) and an unresolved narrow Gaussian line (0.1 keV width). The line was not detected and we obtained an upper limit on the normalization of the line of $< 1.2 \times 10^{-6}$ photons s⁻¹ cm⁻² corresponding to a 3σ upper limit of 780 eV on the line’s equivalent width. We ran simulations, following Protasov et al. (2002), to test for the presence of the iron line, resulting in a p -value of 0.832. This indicated that the spectra are consistent with the absorbed power law model and no additional line is required by the current data. Thus we do not find any strong reflection signatures in the *Chandra* spectrum.

Future high resolution, high S/N spectra with addition of the high energy X-rays are needed for any detection of spectral or reflection features and more detailed study of the X-ray nature of this source.

5. DISCUSSION

5.1. Cocoon model

The overall compact radio morphology of TXS 0128+554 can be attributed to a highly overpressurized cocoon structure that is driving a bow shock into the surrounding galactic medium. In this scenario a thin shell exists around the cocoon and is the site of particle acceleration, with synchrotron emission being produced by the non-thermal electrons. Simple analytical models (e.g., Begelman & Cioffi 1989, Kino & Kawakatu 2005, Stawarz et al. 2008) have been developed to describe the evolution of the cocoon as it is inflated by a relativistic jet outflow. These generally contain several features associated with the jet and counter-jet: a head (hotspot) where the collimated outflow impacts the external medium, and a working surface over which the jet kinetic energy is dissipated. The latter is the leading curved edge of a radio lobe embedded within the cocoon (see, e.g., Fig. 1 of Begel-

³ <https://cxc.harvard.edu/ciao/>

⁴ <http://cxc.harvard.edu/sherpa/>

⁵ <https://cxc.harvard.edu/toolkit/colden.jsp>

⁶ <https://heasarc.gsfc.nasa.gov/xanadu/xspec/manual/XSmodelApec.html>; <http://atomdb.org/>

Table 5. X-ray Spectral Models

Model description ^a	$N_H(z)^b$ (10^{22} cm^{-2})	Γ	kT (keV)	Flux (soft)	Flux (hard)	Cash/d.o.f
PL	0.70 ± 0.08	2.38 ± 0.10		10.8 ± 1.31	$7.04_{-1.23}^{+1.45}$	1669.9/1773
PL + Apec	$0.67_{-0.05}^{+0.08}$	$2.39_{-0.11}^{+0.06}$	< 0.08	11.2 ± 0.22	$7.03_{-0.25}^{+0.31}$	1668.8/1771

^a PL - power law, Apec - thermal hot plasma model, G - Gaussian line; Unabsorbed flux in the soft (0.5-2 keV) and hard (2-10 keV) bands extrapolated from the model fitted over the 0.5-7 keV range, in units of $10^{-13} \text{ erg cm}^{-2} \text{ s}^{-1}$.

^b All models assume the Galactic absorbing column of $2.633 \times 10^{20} \text{ cm}^{-2}$ and redshift $z = 0.0365$ for the intrinsic absorption.

^c Models: 1/ `phabs*zphabs*powerlaw`; 2/ `phabs*zphabs*(powerlaw + apec)`.

man & Cioffi 1989, and Fig. 1 of Croston et al. 2009). The jet head advances at a speed v_h dictated by ram pressure equilibrium, such that $L_j/c = \rho v_h^2 A_h$, where ρ is the external medium density, L_j is the jet kinetic power, c is the speed of light, and A_h is the area of the working surface.

The hotspots of radio galaxies (e.g., Cyg A, see Carilli & Barthel 1996) frequently exhibit a flat or inverted radio spectra ($\alpha > -0.5$), implying that they are principal sites of particle acceleration (Meisenheimer et al. 1989). Such active hotspots are not seen in TXS 0128+554. All of the inverted spectrum regions are located in the bright inner jet region close to the core. Those regions are also bright in the higher-frequency VLBI bands, indicating ongoing particle acceleration. In contrast, the radio lobes of the source have steep-spectra, and their low frequency emission is likely due to an aging population of electrons.

The distinct gap between the inner and outer regions in the VLBI images above 6 GHz leads us to conclude that they are not causally connected. The brightness temperature and steep spectral index of C5 are comparable to the other bright features in the eastern lobe, whereas its radio brightness might be expected to be enhanced if it is actively being energized by the C10-C8 jet. Although the velocity vector of C8 does point to C5, the velocity vectors of these two features are not collinear, suggesting that their similar apparent speeds are merely a coincidence.

We conclude that the jets in TXS 0128+554 turned off for a period during its lifetime, and have subsequently re-started. Such intermittent jet activity has been proposed in theoretical models for young radio sources, e.g., (Reynolds & Begelman 1997; Czerny et al. 2009). The radio lobes are remnants from the initial period of jet activity, while the inner jet (associated with core features

C8, C9 and C10; § 4.3) was launched more recently and is advancing during the present epoch.

In Figure 7 we show a schematic timeline of the jet activity in the source. The marked epochs refer to times in the rest frame of the central engine. The jet was initially launched at t_1 , and turned off at t_j , producing the radio lobes that we see today. The bright C8 radio feature marks the outer edge of a restarted jet that was launched at t_2 . Photons we currently receive from the core region were emitted at $t_{c,\text{now}}$. The shorter light travel distance to the western lobe and its relativistic advance speed imply that its photons were emitted at a later time t_f . Conversely, we see a relatively younger version of the eastern lobe (i.e., at epoch t_b) since it is farther away and receding with respect to its western counterpart. For a constant advance speed, we would expect (Ryle & Longair 1967)

$$t_f = t_{c,\text{now}} / (1 - \beta \cos \theta) = 1.25 t_{c,\text{now}}$$

and

$$t_b = t_{c,\text{now}} / (1 + \beta \cos \theta) = 0.84 t_{c,\text{now}}.$$

Clearly t_j is an important parameter since it (along with $L_{j,1}$) dictates how much total energy has been injected into the lobe structure. Given the young kinematic age of 82 ± 17 y, there is insufficient time for the lobes to experience much spectral ageing at low radio frequencies, and we see little indication of curvature in our radio spectra of the bright lobe features. Assuming a magnetic field strength typical of CSOs, a spectral downturn would occur at 22 GHz in the lobes of TXS 0128+554 only after ~ 1700 y (Pacholczyk 1970).

We can place a conservative lower limit on the duration of the initial period of jet activity by equating the source cavity enthalpy to the energy injected during the initial epoch of jet activity, i.e., $4pV = L_{j,1}(t_j - t_1)$. If we were to assume that the maximum jet kinetic luminosity TXS 0128+554 could have had in this phase

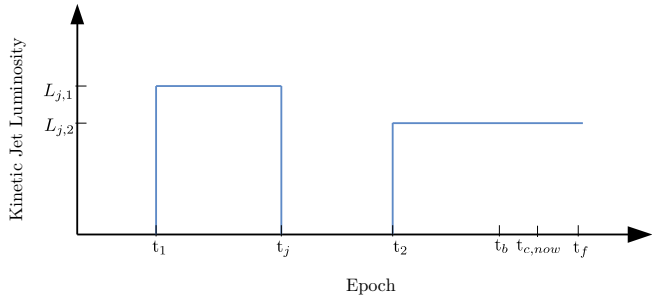


Figure 7. Schematic diagram of the evolution of kinetic jet luminosity in TXS 0128+554 with times in the rest frame of the central engine (in arbitrary units and not to scale). The first jet turn-off happened at a time t_j after its initial birth at t_1 . A period of jet inactivity lasted until the jet re-started at t_2 . The latter event generated the bright ~ 2 mas long inner jet visible in the VLBA 15.4 GHz image at the current epoch $t_{c,now}$. Due to light time delays and the relativistic expansion speeds, radiation from the western (approaching) lobe, which originated from the initial jet activity epoch, is seen at a later epoch than the core emission, while the eastern (receding) lobe is viewed at an earlier epoch than the core.

was equal to that of the most powerful known CSOs ($L_{j,1} \simeq 10^{45} \text{ erg s}^{-1}$; Wójtowicz et al. 2020), we find $t_j - t_1 \geq 2.7$ y.

We apply the model of Stawarz et al. (2008) to the first epoch of jet activity which is responsible for production of the outer radio lobes. Here the jet kinetic power is constant over time, and the external medium has a flat density profile $\rho = m_p n_o$, where m_p is the proton mass and $n_o = 0.1 \text{ cm}^{-3}$ (typical for CSO environments). This leads to a constant head advance speed over time. This is a reasonable assumption as we see no evidence of a significant change in speed in the moving features over the three year period of the MOJAVE 15 GHz VLBA observations, and over a 10 year period at 8 GHz (§ 4.3).

The energy transported by the jet is transformed into the cocoon’s internal pressure p , which also causes it to expand sideways with a velocity $v_c = (p/\rho)^{1/2}$. Additionally, the transverse size l_c is taken to vary with time as $l_c \propto t^{1/2}$, so as to reproduce the ballistic phase of jet advance, following the numerical simulations of Scheck et al. (2002). The model has three free parameters: v_h , l_c , and the linear size (LS), with the latter being defined as the separation of the jet head from the core. From the observations, the parameter values at epoch t_f are $v_h = 0.32 \pm 0.07$ c, $l_c = 2.87 \pm 0.36$ pc, and $LS = 5.67 \pm 0.65$ pc. This yields a jet kinetic power of $(1.28 \pm 1.16) \times 10^{43} \text{ erg s}^{-1}$, which agrees to within an order of magnitude with the predicted value based on previously published correlations with jet radio luminosity (Willott et al. 1999; Daly et al. 2012). We note that this is an estimate of the jet kinetic power $L_{j,1}$ of

the initial jet activity epoch ($t_1 < t < t_j$) only, since this method takes into consideration the features of the lobes only and not the (re-started) inner jet.

The radio emission from the lobes, as in other GPS/CSS sources, is most likely of synchrotron origin. The lobe is injected with freshly accelerated electrons from the terminal jet hotspot, which then undergo adiabatic and radiative cooling. We assume a power-law energy distribution injection function that stays fairly constant with time during the initial jet activity (ballistic expansion) phase. By further assuming the electron energy density to be in rough equipartition with the magnetic energy density and lobe pressure, the lobe synchrotron luminosity is predicted to be $\log L = 41 \pm 1 \text{ erg s}^{-1}$. This is in agreement with the integrated radio luminosity, $2.8 \times 10^{41} \text{ erg s}^{-1}$, which we obtained by fitting a single component synchrotron self-absorption (SSA) model to the single dish and VLBI radio flux densities as plotted in Figure 2. The fit yields a SSA turnover frequency of ~ 657 MHz, which is in agreement with the ~ 630 MHz turnover that is predicted by the Stawarz et al. (2008) cocoon model.

Equipartition magnetic field estimates based on a spherical cocoon geometry (e.g., Orienti & Dallacasa 2012; Pacholczyk 1970) yield values in the range 3-9 mG. The Stawarz et al. (2008) cocoon model yields a similar range: ~ 5 -20 mG, depending on the choices for the magnetic field and electron energy equipartition parameters η_B and η_e . This is comparable to the typical range of 1-10 mG measured in GPS and CSO galaxies (Dallacasa et al. 2002, Orienti et al. 2006).

It is somewhat surprising that TXS 0128+554 lies significantly outside the well-studied trend between turnover frequency and linear size (e.g., O’Dea & Baum 1997), which would predict a much higher turnover frequency of ~ 50 GHz. Tornainen et al. (2008) found a cluster of several GPS sources that lie in a similar location in the turnover – linear size plane. In the case of TXS 0128+554 this may be due to the fact that the outer lobes have not been re-supplied by the central AGN for some time, which has affected their overall evolution and radio properties.

With a 150 MHz radio luminosity of only $10^{23.6} \text{ W Hz}^{-1}$, TXS 0128+554 is at the low end of the luminosity range of a large sample of over 23 000 AGN from the LO-FAR 1st data release studied by Hardcastle et al. (2019). These authors found that most AGN in the luminosity range $10^{25} < L_{150} < 10^{27} \text{ W Hz}^{-1}$ are long-lived objects in relatively poor (group-like) environments, and there are relatively few physically small objects in this luminosity range. The large number of small objects at lower luminosities led them to conclude that they

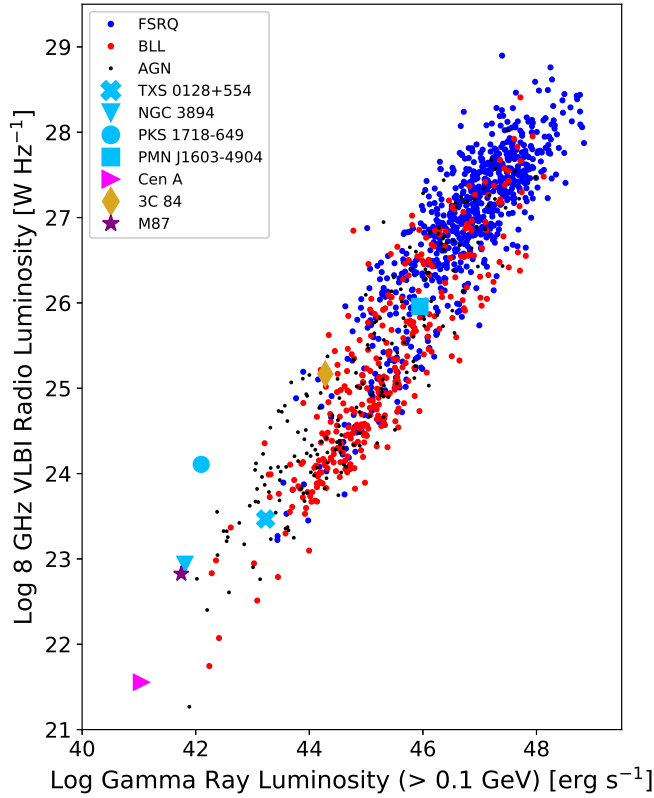


Figure 8. Plot of VLBI 8 GHz luminosity versus γ -ray luminosity (> 0.1 GeV) for AGN in the 4LAC catalog. Small red circles denote BL Lac objects, small blue circles denote flat-spectrum radio quasars, and black dots denote other AGN. The blue cross denotes TXS 0128+554, and large light blue symbols represent *Fermi*-detected CSOs. The other large symbols denote selected nearby radio galaxies detected by *Fermi*.

must either have a different lifetime distribution, or different jet physics from the more powerful objects. It may be possible, therefore, that many weak AGN like TXS 0128+554 never grow to large sizes, due to their episodic/short-lived jet activity.

5.2. Origin of the high-energy emission

Stawarz et al. (2008) predict that the lobes in powerful GPS/CSS sources should also emit significant γ -ray emission via inverse Comptonization of seed photons by the lobe electrons. Stellar emission in the near-IR from the host galaxy, synchrotron emission from the lobe electrons, IR radiation from the dusty torus, UV radiation from the accretion disk and cosmic microwave background radiation are considered to be the main components for the seed photon field. However, when applied to our source, the model under-predicts the γ -ray flux observed by *Fermi*-LAT by three orders of magnitude. We therefore conclude that it is highly unlikely that the

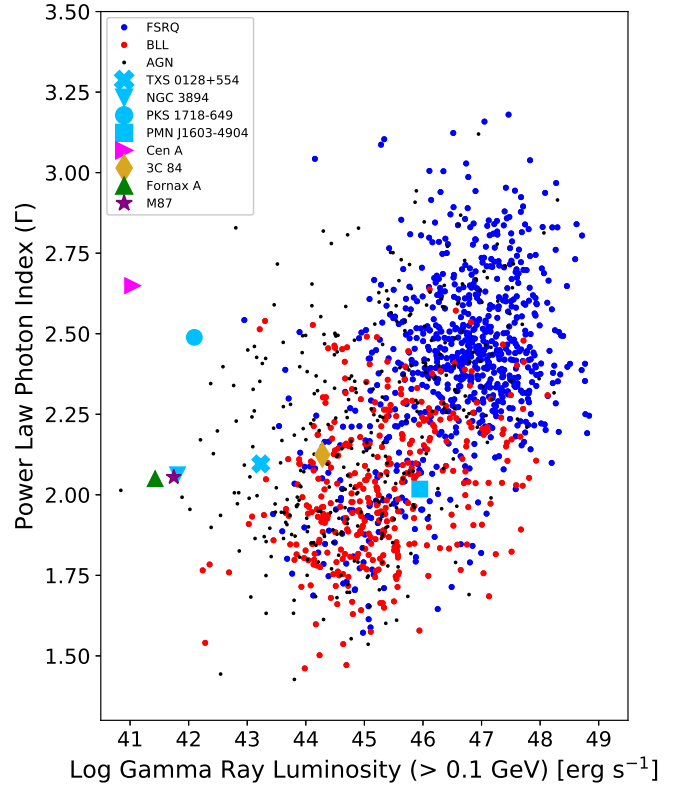


Figure 9. Plot of power law photon index versus γ -ray luminosity (> 0.1 GeV) for AGN in the 4LAC catalog. Small red circles denote BL Lac objects, small blue circles denote flat-spectrum radio quasars, and black dots denote other AGN. The blue cross denotes TXS 0128+554, and large light blue symbols represent *Fermi*-detected CSOs. The other large symbols denote selected nearby radio galaxies detected by *Fermi*.

observed γ -ray emission of TXS 0128+554 originates in its lobes.

The other possible sources of X-rays and γ -rays are the inner jet/optically thick core region and a shocked shell surrounding the cocoon. We can compare the un-absorbed X-ray luminosities of the cores and bright knots or hotspots of some of well-known, *Chandra*-resolved jets to that of TXS 0128+554 to examine whether the majority of the high energy emission may originate in the radio-loud inner core. We consider the cases of M87 and Cen A, which are both nearby and well-resolved in X-rays. The core of M87 has a luminosity of 4.4×10^{40} erg s $^{-1}$ in the 0.5–10 keV band (Marshall et al. 2002), while the HST-1 feature reached an order of higher magnitude X-ray luminosity during a large flare (Harris et al. 2006). Cen A is slightly more luminous in X-rays; the nucleus has a luminosity of 5×10^{41} erg s $^{-1}$ in the 2–10 keV band (Kraft et al. 2000) while the brighter knots have luminosities of the order of 10^{38} – 10^{39} erg s $^{-1}$ in the 0.1–10 keV band (Kraft

et al. 2001). Hence, when compared to the unbeamed X-ray luminosity of TXS 0128+554 ($2.30 \times 10^{42} \text{ erg s}^{-1}$ and $1.51 \times 10^{42} \text{ erg s}^{-1}$ in the 0.5–2 keV and 2–10 keV bands, respectively), it is plausible that the core is the major source of the high energy emission.

We note that the shell surrounding the south-west lobe of Cen A has also been observed to emit strongly in X-rays ($\sim 10^{38} \text{ erg s}^{-1}$), and the majority of the X-ray emission has been shown to be non-thermal (Croston et al. 2009). The jet power of Cen A, calculated from the size of the cavity excavated by the jets, is found to be $\sim 10^{43} \text{ erg s}^{-1}$. This is similar to that of TXS 0128+554, although Cen A is considerably older, with a kinematic age of $\sim 2 \times 10^6$ years.

5.3. Comparison of TXS 0128+554 with other CSOs

TXS 0128+554 is the fourth confirmed CSO to be detected in γ -rays by the *Fermi* LAT instrument. Current CSO catalogs (e.g., Tremblay et al. 2016) contain on the order of ~ 50 AGN, making the *Fermi*-detected ones a very rare subset. With the exception of PMN J1603–4904 at $z = 0.232$ (see discussion of the redshift in the Appendix), all of the *Fermi* CSOs are at redshift less than $z < 0.04$. In Figure 8 we plot 8 GHz radio luminosity versus γ -ray luminosity for all 4FGL AGN with a known redshift and a compact radio luminosity tabulated in the radio fundamental catalog⁷), which is complete down to approximately 150 mJy (Kovalev et al. 2007; Petrov et al. 2008). Most GPS and CSO AGN are not detected by *Fermi*, yet have radio luminosities in the 10^{27} to $10^{28} \text{ W Hz}^{-1}$ range, comparable to the flat-spectrum blazars that dominate the *Fermi* catalogs. TXS 0128+0554 and two of the other *Fermi* CSOs have considerably lower radio powers, however, and lie among the lowest γ -ray luminosity AGN detected so far by *Fermi*.

The detection of AGN by the LAT instrument is strongly influenced by the spectral hardness (photon index Γ) of the source in the γ -ray regime. Weak-lined BL Lac objects tend to have harder γ -ray spectra (lower Γ) than flat-spectrum radio quasars, and are therefore detectable to lower flux levels. This is illustrated in Figure 9, where we present an updated version of the Principe et al. (2020) plot of photon index versus γ -ray luminosity for all AGN in the 4LAC catalog (The *Fermi*-LAT collaboration 2019). The large light blue symbols represent the *Fermi* CSOs, with the blue cross denoting TXS 0128+554. We have also highlighted several nearby *Fermi*-detected radio galaxies in the plot for compari-

son. Cen A is among the closest jetted AGN and along with Fornax A are the only AGN where *Fermi* has resolved γ -ray emission from the jet lobe structure (Abdo et al. (2010); Ackermann et al. (2016)). M87 is a nearby well-studied jetted AGN in the Virgo cluster that lies in the same location in the Γ - L_γ plane as Fornax A and the CSO NGC 3894.

The large luminosity of PMN J1603–4904 clearly sets it apart from the other CSOs and nearby radio galaxies in Fig. 9, as its γ -ray properties have more in common with the BL Lac objects. Its spectral energy distribution is strongly Compton-dominated, and its γ -ray emission is known to be highly variable (Abdo et al. 2009; Krauß et al. 2018). We have included the radio galaxy 3C 84, another highly variable γ -ray emitter, in the plot, as it presents an interesting case of restarted jet activity in its core, marked by large radio outbursts occurring in 1960 and 2005 (Nagai et al. 2014). The former event led to the production of two CSO-like mini-lobes that are expanding supersonically into the surrounding medium (Kino et al. 2017). There has been considerable debate as to the source of the γ -ray rays in 3C 84, which may originate in the inner jet (Giovannini et al. 2018) and/or its pc-scale lobes. Its jets show only mildly relativistic motion (0.4c; Lister et al. 2019), and the radio morphology, free-free absorption, and kinematics of the lobe emission suggest a high viewing angle of 60° (Fujita & Nagai 2017).

Despite the relatively low levels of Doppler boosting in 3C 84 and TXS 0128+554, they both lie near the region populated by BL Lac objects in Figure 9. Along with PMN J1603–4904, they have substantially higher γ -ray luminosities than the other CSOs. It is likely that their strong γ -ray emission may be associated with a heightened activity state near the base of the jet, which is associated with their recently launched jets. A similar conclusion was reached by Principe et al. (2020) in their comparison of NGC 3894 to other CSOs and *Fermi*-detected AGN.

In Table 6 and Table 7 we have compiled information on all *Fermi*-detected and other confirmed CSOs in the literature with $z < 0.1$. We provide detailed individual descriptions of these sources in the Appendix. This is not likely a complete list, as new CSOs (such as TXS 0128+554) are still being discovered. In particular, we have omitted three AGN that have been proposed as CSOs by Tremblay et al. (2016): VIPS J09062+4636, VIPS J11488+5924, VIPS J12201+2916, since they do not have published kinematic ages. We have also excluded the compact AGN OQ 208, as it has shown a significant radio flux density decline by a factor of ~ 4.5 since 2000, which is highly atypical of CSOs (e.g., Fass-

⁷ <http://astrogeo.org/rfc/>

Table 6. Properties of *Fermi*-Detected and Other Nearby CSO Galaxies

Source Name	z	D_L [Mpc]	Host Galaxy	kpc morph.	LLS [pc]	θ [$^\circ$]	β_{app} [c]	Age [y]	ν_m [GHz]	f
(1)	(2)	(3)	(4)	(5)	(6)	(7)	(8)	(9)	(10)	(11)
<i>Fermi</i> -detected CSOs										
TXS 0128+554	0.036	159	Elliptical	C	12	52^{+7}_{-9}	0.32 ± 0.07	82 ± 17	0.66	0.48
NGC 3894	0.011	47	Elliptical	E	7	10–21	~ 0.1	59 ± 5	5	0.18
PKS 1718–649	0.014	62	Elliptical ^a	C	2.5	...	0.06 ± 0.03	70 ± 30	3.6	< 0.01
PMN J1603–4904	0.232	1148	Unknown ^b	E	56	...	< 3	> 54	0.39	0.37
Low Redshift CSOs Lacking <i>Fermi</i> LAT Associations										
4C 31.04	0.060	266	Elliptical	C	100	75–80	0.34	550	0.4	0.016
PMN J1511+0518	0.084	378	Elliptical	C	11	...	0.28	55	10	0.03
B2 0035+22	0.096	435	Elliptical	C	22	...	0.5	450	0.4–1.4	0.014

^a Host has an elliptical nucleus with a prominent dust lane, surrounded by faint spiral structure.

^b No indications of active star formation in optical spectrum (Goldoni et al. 2016).

NOTE—Columns are as follows: (1) source name, (2) redshift, (3) luminosity distance in Mpc, (4) host galaxy type, (5) kpc scale radio morphology, where E = extended, and C = compact, (6) largest projected linear size of inner jet structure as measured from hotspot-to-hotspot in pc, (7) jet viewing angle in degrees, (8) apparent expansion speed in units of the speed of light, (9) dynamical age of the radio source in years, (10) radio spectral turnover frequency in GHz, (11) ratio of core flux density to total flux density at 8 GHz.

Table 7. Spectral Properties of *Fermi*-Detected and Other Nearby CSO galaxies

Source Name	$\log L_\nu$ (1.4 GHz) [W Hz ⁻¹]	$\log \nu L_\nu$ (0.5–2 keV) [erg s ⁻¹]	$\log \nu L_\nu$ (2–10 keV) [erg s ⁻¹]	$\log \nu L_\nu$ (0.1–100 GeV) [erg s ⁻¹]	Γ (0.1–100 GeV)	$\log \nu L_\nu$ (10–1000 GeV) [erg s ⁻¹]	Γ (10–1000 GeV)
(1)	(2)	(3)	(4)	(5)	(6)	(7)	(8)
<i>Fermi</i> -detected CSOs							
TXS 0128+554	23.7	42.5	42.3	43.2	2.10 ± 0.09	42.5	3.1 ± 0.9
NGC 3894	23.1	40.5 ^a	40.8	41.8	2.06 ± 0.12
PKS 1718–649	24.3	40.9	41.2	42.1	2.49 ± 0.18
PMN J1603–4904	26.3	43.5	43.6	45.9	2.02 ± 0.03	45.6	2.2 ± 0.10
Low Redshift CSOs Lacking <i>Fermi</i> LAT Associations							
4C 31.04	25.3	< 40.6
PMN J1511+0518	25.2	42.0	42.7
B2 0035+22	25.1	41.6	41.9

^a 0.7–2 keV luminosity.

NOTE—Columns are as follows: (1) source name, (2) log of 1.4 GHz luminosity (L_ν) in W Hz⁻¹, (3) log of 0.5–2 keV x-ray luminosity in erg s⁻¹, (4) log of 2–10 keV x-ray luminosity (νL_ν) in erg s⁻¹, (5) log of 0.1–100 GeV γ -ray luminosity from 4FGL in erg s⁻¹, (6) 4FGL power law photon index between 0.1 and 100 GeV, (7) log of 10–1000 GeV γ -ray luminosity from 3FHL in erg s⁻¹, (8) 3FHL power law photon index between 10 and 1000 GeV.

nacht & Taylor 2001). The three CSOs with $z < 0.1$ that do not have *Fermi* LAT detections are 4C 31.04, PMN J1511+0518, and B2 0035+22.

Comparing the properties of the nearby non-*Fermi* detected CSOs, all have low pc-scale core fractions, which is typical for members of this AGN class (Stanghellini et al. 2001). Whereas 4C 31.04 and B2 0035+22 both have kinematic ages of ~ 500 y, roughly an order of magnitude larger than the *Fermi*-detected CSOs, PMN J1511+0518 has a relatively young age of only 55 y. It has an X-ray luminosity comparable to TXS 0128+554 and would be a strong candidate for future detection by the *Fermi* LAT instrument.

6. SUMMARY

We have performed a *Chandra* X-ray and multi-frequency radio VLBA study of the AGN TXS 0128+554, which is associated with the *Fermi* γ -ray source 4FGL J0131.2+5547. We summarize our major findings as follows:

(i) Our multi-frequency VLBA observations between 2.3 GHz and 22.2 GHz reveal a compact radio structure typical of the compact symmetric object (CSO) class. Archival VLA and published GMRT observations indicate no extended radio emission on kpc-scales. On pc-scales the emission consists of a strong flat-spectrum core flanked by two steep-spectrum lobes, with a diameter of approximately 11 pc, that extends to ~ 16 pc at the lowest observing frequencies.

(ii) The flat-spectrum core is atypically bright compared to the lobes for a typical CSO, and shows no apparent shift in position (upper limit = 0.03 mas) between 5.0 GHz and 22.2 GHz. The cores of most compact blazars typically show shifts of ~ 0.3 mas over this frequency range due to opacity effects. This suggests that the core feature in TXS 0128+554 is not the optically thick $\tau = 1$ surface, but rather a recollimation or reconfinement shock.

(iii) We analyzed 7 additional 15 GHz epochs from the MOJAVE archive, and found significant proper motions for three features over a three year period. The bright features C5 and C8 in the approaching (western) lobe are moving away from the core with apparent speeds of $0.32c \pm 0.07c$ and $0.28c \pm 0.06c$, respectively. Feature C1 in the receding lobe has an apparent motion of $0.174c \pm 0.042c$ toward the core.

(iv) The relativistic expansion speeds suggest that the emission from the approaching and receding effects suffers from time delay effects, and are viewed at different epochs than photons from the core region of the source. By assuming intrinsic symmetry in the lobes, we used the apparent size and flux density asymmetry

in the VLBA images to determine a jet axis viewing angle of 52_{-9}^{+7} degrees, and an intrinsic expansion speed of $0.32_{-0.07}^{+0.08}c$. This implies only mild Doppler boosting factors of $\delta = 1.2$ in the approaching jet and $\delta = 0.79$ in the counter-jet.

(v) Under the assumption of a constant advance speed in the western lobe, we derive a kinematic age of 82 ± 17 y, placing TXS 0128+554 among the youngest known relativistic AGN jet systems.

(vi) We detected TXS 0128+554 in our targeted 19.3 ks *Chandra* ACIS-S imaging observations, and the structure is consistent with an unresolved point source. The spectrum between 0.5 keV and 7 keV is well fit by an absorbed power law model with photon index $\Gamma = 2.38 \pm 0.10$. The fitted absorbing column of $N_H(z) = 6.7 \times 10^{21} \text{ cm}^{-2}$ is in agreement with the expected H I absorbing column density predicted from the $N_{\text{HI}} - \text{linear size relation}$, as well as the trend between source size, radio luminosity and absorbing column studied by Sobolewska et al. (2019). We do not find evidence for a spectral feature at 6.4 keV that would be due to the presence of a reflection of the primary absorbed X-ray radiation off a cold medium. The relatively soft X-ray spectrum compared to other X-ray detected CSOs may be indicative of a thermal emission component, for which we were able to obtain an upper temperature limit of $kT = 0.08$ keV.

(vii) A distinct emission gap between the bright inner jet and the outer lobe structure, as well as the lack of compact, inverted-spectrum hotspots indicate that TXS 0128+554 has undergone pc-scale episodic jet activity. The jets originally became active approximately 90 y ago, producing and energizing the outer lobe structures. After a period of quiescence, the jets were re-launched roughly 10 y ago, producing the bright inner jet features and increasing the synchrotron emission from the compact core. Intermittent jet activity has been proposed (Reynolds & Begelman 1997; Czerny et al. 2009) and observed in young radio sources (Owsianik et al. 1998). TXS 0128+554 is the first CSO with a measured kinematic age which can potentially provide constraints on the theoretical models.

(viii) The 1.4 GHz radio luminosities of TXS 0128+554 and two of three other *Fermi*-detected CSOs are in the range of $10^{23} \text{ W Hz}^{-1}$ to $10^{24} \text{ W Hz}^{-1}$, several orders of magnitude below the typical values for CSOs. These two γ -ray CSOs: NGC 3894, PKS 1718–649, both have redshifts below 0.02, while the third γ -ray CSO, PMN J1603–4904 has a redshift of 0.23, based on three blended lines in a near-featureless spectrum (Goldoni et al. 2016). Comparing the properties of the γ -ray CSOs to three other known CSOs

with $z < 0.1$, the latter have radio powers of $\sim 10^{25}$ W Hz $^{-1}$ and very weak/non-detected core features. We therefore find support for the suggestion put forward by Principe et al. (2020) that the γ -ray emission in these CSOs is originating in the core region, and is a hallmark of recently started jet activity. Indeed, a fit to our measured properties of TXS 0128+554 based on the high-energy inverse Compton model of Stawarz et al. (2008) predicts a γ -ray lobe (cocoon) luminosity that is three orders of magnitude lower than that observed by *Fermi*.

ACKNOWLEDGMENTS

We thank Alexander V. Plavin, Eduardo Ros, and the anonymous referee for useful suggestions on the manuscript. This work was supported by NASA-*Fermi* grant 80NSSC17K0517, NASA-*Chandra* grant GO9-20085X, and NASA contract NAS8-03060 (*Chandra* X-ray Center). YK and AB were supported by the Russian Science Foundation grant 16-12-10481. The MOJAVE project was supported by NASA-*Fermi* grants NNX08AV67G, NNX12A087G, NNX15AU76G, and 80NSSC19K1579.

The Very Long Baseline Array and the National Radio Astronomy Observatory are facilities of the National

Science Foundation operated under cooperative agreement by Associated Universities, Inc. This work made use of the Swinburne University of Technology software correlator (Deller et al. 2011), developed as part of the Australian Major National Research Facilities Programme and operated under licence. This research has made use of data from the OVRO 40-m monitoring program Richards et al. (2011), which is supported in part by NASA grants NNX08AW31G, NNX11A043G, and NNX14AQ89G as well as NSF grants AST-0808050 and AST-1109911. This research has made use of the NASA/IPAC Extragalactic Database (NED) which is operated by the Jet Propulsion Laboratory, California Institute of Technology, under contract with the National Aeronautics and Space Administration. The authors made use of the database CATS Verkhodanov et al. (2005) of the Special Astrophysical Observatory. This research has made use of data obtained by the *Chandra* X-ray Observatory, and software provided by the *Chandra* X-ray Center (CXC) in the application packages CIAO and *Sherpa*.

Facilities: VLBA, *Chandra*, *Fermi*.

APPENDIX

A. LOW-REDSHIFT CSOS DETECTED BY *Fermi*

PKS 1718–649: This was the first reported γ -ray loud CSO (Migliori et al. 2016), and is located in the nucleus of the nearby ($z = 0.014$) galaxy NGC 6328 which has a LINER type optical spectrum (Filippenko 1985). The galaxy has a bright nuclear elliptical region, a prominent dust lane, and faint outer spiral structure that may be indicative of an ongoing merger (Fanti et al. 2000; Maccagni et al. 2018). The AGN is embedded in a dense nuclear gas environment, and exhibits radio spectral variability associated with free-free absorption (Tingay et al. 2015). It has been studied in X-rays with *Chandra* (Siemiginowska et al. 2016) and *XMM-Newton* (Beuchert et al. 2018). The 8.4 GHz and 22 GHz VLBI observations of Angioni et al. (2019) show two bright lobes with a projected separation of only 2.5 pc. They suggest the core is located in between these lobes, in a region with an inverted spectrum, but its precise location could not be determined. The lack of long term flux density variability and overall GPS spectrum led Tingay et al. (2002) to classify the source as a CSO, which is confirmed by Angioni et al. (2019). Giroletti & Polatidis (2009) reported a lobe advance speed of 0.07 c and a kinematic age of 91 y. The multi-epoch TANAMI observations obtain a kinematic age of (70 ± 30) y, based on the observed hot spot separation rate of (0.13 ± 0.06) mas y^{-1} . Assuming symmetry, this gives a lobe advance speed of $0.06 c \pm 0.03 c$.

NGC 3894: This low-luminosity CSO is located in an elliptical galaxy at $z = 0.01075$, and was found to be γ -ray loud by Principe et al. (2020) after stacking 10.8 y of Pass 8 *Fermi* LAT data. The 5 GHz VLA image of Taylor et al. (1998) shows a bright core flanked by radio lobes separated by ~ 800 pc. On mas scales, the flat spectrum core is flanked by two bright, continuous jets with projected lengths of ~ 2 pc (Tremblay et al. 2016). Fainter diffuse emission is visible in both jets farther from the core in low-frequency VLBI images (Taylor et al. 1998). The inner radio source has a high core fraction ($f = 0.18$). Principe et al. (2020) find expansion speeds of $\sim 0.1 c$ and a viewing angle of $10^\circ \leq \theta < 21^\circ$ for the inner jets. These measurements imply a young kinematic age of 59 ± 5 y.

PMN J1603–4904: This AGN is associated with a bright and variable Fermi LAT γ -ray source with a strongly Compton-dominant spectral energy distribution and hard photon index above 10 GeV (Krauß et al. 2018). The source is located at low galactic latitude, and VLT/X-Shooter spectrographic observations by Goldoni et al. (2016) revealed a blazar-like, non-stellar optical/NIR continuum with no apparent contribution from the host galaxy. They detected a blended H α -[NII] complex at 8100 Å, and two blended [SII] lines at 8250 Å, as well as a much fainter emission line in the NIR. The few detectable spectral lines led them to classify the source as a radio galaxy powered by a LINER/Seyfert nucleus. The observed turnover in the radio spectrum at ~ 400 MHz (Müller et al. 2016) and the small overall extent of the VLBI radio emission (Müller et al. 2014) have led to a CSO classification for the source. Müller et al. (2016) concluded that the source must also have larger scale low-frequency radio emission based on comparisons with single dish flux density measurements. Multi-epoch VLBI observations by the TANAMI collaboration (Müller et al. 2014) show a central feature flanked by two hotspots with separation ~ 50 pc, with continuous jet emission in between them. They set a limit of < 3 c on any possible expansion speed.

B. LOW-REDSHIFT CSOS NOT DETECTED BY *Fermi*

4C 31.04: This AGN is located in a nearby ($z = 0.059$) giant elliptical galaxy and is interacting with dense gas associated with a 2 kpc diameter circumnuclear disk (Zovaro et al. 2019; Struve & Conway 2012). Its radio structure consists of a flat spectrum core flanked by two radio lobes, with an overall diameter of ~ 100 pc. Giovannini et al. (2001) estimate a viewing angle of 75 to 80 degrees for the jets from the line of sight. The integrated radio spectrum is peaked at ~ 400 MHz. Both radio lobes have compact hotspots, and the flat spectrum core contains a typically small fraction ($f = 0.016$) of the total mas-scale flux density. Giroletti et al. (2003) measured a lobe advance velocity of $0.34c$ based on two VLBI epochs, and obtained a kinematic age of 550 y. However Zovaro et al. (2019) derived a much larger value (≥ 12 ky) using the bubble expansion model of Bicknell & Begelman (1996).

PMN J1511+0518: This nearby Seyfert I galaxy ($z = 0.084$) has a simple two-sided compact radio structure, with a flat-spectrum core flanked by two hotspot-dominated lobes separated by 11 pc on the sky (Hovatta et al. 2014). Low-frequency VLBI images show additional diffuse lobe emission to the southeast of the eastern hotspot, roughly 60 pc from the core, that may be a relic of previous jet activity (Oriente & Dallacasa 2008). The eastern hot spot is moving steadily in a non-radial direction away from the core, at an apparent speed of 0.285 ± 0.024 c, according to multi-epoch 15 GHz MOJAVE VLBA observations (Lister et al., in prep.). This yields a kinematic age of 55 y. PMN J1511+0518 has a low core fraction ($f = 0.03$) and belongs to the high-frequency peaker class, with a turnover in its integrated spectrum occurring at ~ 10 GHz (Oriente & Dallacasa 2008).

B2 0035+22: The radio source is hosted by a passive elliptical galaxy at $z = 0.096$ and has a compact triple radio structure 22 pc in diameter, with hotspots in each lobe connected to the flat spectrum central core by a continuous bridge of jet emission. The radio emission is unpolarized, typical of the CSO class (Bondi et al. 2004). Polatidis (2009) measured an expansion velocity of $0.5c$ for the most prominent hotspot and a kinematic age of ~ 450 y. The source is not core-dominated ($f = 0.014$), and has a turnover frequency between 0.4 and 1.4 GHz (An & Baan 2012).

REFERENCES

- Abdo, A. A., Ackermann, M., Ajello, M., et al. 2009, ApJ, 699, 31, doi: [10.1088/0004-637X/699/1/31](https://doi.org/10.1088/0004-637X/699/1/31)
- . 2010, Science, 328, 725, doi: [10.1126/science.1184656](https://doi.org/10.1126/science.1184656)
- Abdollahi, S., Acero, F., Ackermann, M., et al. 2020, ApJS, 247, 33, doi: [10.3847/1538-4365/ab6bcb](https://doi.org/10.3847/1538-4365/ab6bcb)
- Acero, F., Ackermann, M., Ajello, M., et al. 2015, ApJS, 218, 23, doi: [10.1088/0067-0049/218/2/23](https://doi.org/10.1088/0067-0049/218/2/23)
- Ackermann, M., Ajello, M., Atwood, W. B., et al. 2015, ApJ, 810, 14, doi: [10.1088/0004-637X/810/1/14](https://doi.org/10.1088/0004-637X/810/1/14)
- Ackermann, M., Ajello, M., Baldini, L., et al. 2016, ApJ, 826, 1, doi: [10.3847/0004-637X/826/1/1](https://doi.org/10.3847/0004-637X/826/1/1)
- Ajello, M., Atwood, W. B., Baldini, L., et al. 2017, ApJS, 232, 18, doi: [10.3847/1538-4365/aa8221](https://doi.org/10.3847/1538-4365/aa8221)
- Aller, M. F., Aller, H. D., & Hughes, P. A. 2003, ApJ, 586, 33, doi: [10.1086/367538](https://doi.org/10.1086/367538)
- An, T., & Baan, W. A. 2012, ApJ, 760, 77, doi: [10.1088/0004-637X/760/1/77](https://doi.org/10.1088/0004-637X/760/1/77)
- Angioni, R., Ros, E., Kadler, M., et al. 2019, A&A, 627, A148, doi: [10.1051/0004-6361/201935697](https://doi.org/10.1051/0004-6361/201935697)
- Begelman, M. C., & Cioffi, D. F. 1989, ApJL, 345, L21, doi: [10.1086/185542](https://doi.org/10.1086/185542)
- Beuchert, T., Rodríguez-Ardila, A., Moss, V. A., et al. 2018, A&A, 612, L4, doi: [10.1051/0004-6361/201833064](https://doi.org/10.1051/0004-6361/201833064)
- Bicknell, G. V., & Begelman, M. C. 1996, ApJ, 467, 597, doi: [10.1086/177636](https://doi.org/10.1086/177636)

- Bondi, M., Marchã, M. J. M., Polatidis, A., et al. 2004, *MNRAS*, 352, 112, doi: [10.1111/j.1365-2966.2004.07903.x](https://doi.org/10.1111/j.1365-2966.2004.07903.x)
- Carilli, C. L., & Barthel, P. D. 1996, *A&A Rv*, 7, 1, doi: [10.1007/s001590050001](https://doi.org/10.1007/s001590050001)
- Cash, W. 1979, *ApJ*, 228, 939, doi: [10.1086/156922](https://doi.org/10.1086/156922)
- Cohen, M. H., Meier, D. L., Arshakian, T. G., et al. 2014, *ApJ*, 787, 151, doi: [10.1088/0004-637X/787/2/151](https://doi.org/10.1088/0004-637X/787/2/151)
- Condon, J. J., Cotton, W. D., Greisen, E. W., et al. 1998, *AJ*, 115, 1693, doi: [10.1086/300337](https://doi.org/10.1086/300337)
- Croston, J. H., Kraft, R. P., Hardcastle, M. J., et al. 2009, *MNRAS*, 395, 1999, doi: [10.1111/j.1365-2966.2009.14715.x](https://doi.org/10.1111/j.1365-2966.2009.14715.x)
- Czerny, B., Siemiginowska, A., Janiuk, A., Nikiel-Wroczyński, B., & Stawarz, L. 2009, *ApJ*, 698, 840, doi: [10.1088/0004-637X/698/1/840](https://doi.org/10.1088/0004-637X/698/1/840)
- Dallacasa, D., Orienti, M., Fanti, C., Fanti, R., & Stanghellini, C. 2013, *MNRAS*, 433, 147, doi: [10.1093/mnras/stt710](https://doi.org/10.1093/mnras/stt710)
- Dallacasa, D., Tinti, S., Fanti, C., et al. 2002, *A&A*, 389, 115, doi: [10.1051/0004-6361:20020576](https://doi.org/10.1051/0004-6361:20020576)
- Daly, R. A., Sprinkle, T. B., O’Dea, C. P., Kharb, P., & Baum, S. A. 2012, *MNRAS*, 423, 2498, doi: [10.1111/j.1365-2966.2012.21060.x](https://doi.org/10.1111/j.1365-2966.2012.21060.x)
- Deller, A. T., Brisken, W. F., Phillips, C. J., et al. 2011, *PASP*, 123, 275, doi: [10.1086/658907](https://doi.org/10.1086/658907)
- Fanti, C., Pozzi, F., Fanti, R., et al. 2000, *A&A*, 358, 499. <https://arxiv.org/abs/astro-ph/0005035>
- Fassnacht, C. D., & Taylor, G. B. 2001, *AJ*, 122, 1661, doi: [10.1086/322112](https://doi.org/10.1086/322112)
- Filippenko, A. V. 1985, *ApJ*, 289, 475, doi: [10.1086/162909](https://doi.org/10.1086/162909)
- Fomalont, E. B. 1999, in *Astronomical Society of the Pacific Conference Series*, Vol. 180, *Synthesis Imaging in Radio Astronomy II*, ed. G. B. Taylor, C. L. Carilli, & R. A. Perley, 301
- Freeman, P., Doe, S., & Siemiginowska, A. 2001, *Society of Photo-Optical Instrumentation Engineers (SPIE) Conference Series*, Vol. 4477, *Sherpa: a mission-independent data analysis application*, ed. J.-L. Starck & F. D. Murtagh, 76–87, doi: [10.1117/12.447161](https://doi.org/10.1117/12.447161)
- Fromm, C. M., Ros, E., Perucho, M., et al. 2013, *A&A*, 557, A105, doi: [10.1051/0004-6361/201321784](https://doi.org/10.1051/0004-6361/201321784)
- Fruscione, A., McDowell, J. C., Allen, G. E., et al. 2006, *Society of Photo-Optical Instrumentation Engineers (SPIE) Conference Series*, Vol. 6270, *CIAO: Chandra’s data analysis system*, 62701V, doi: [10.1117/12.671760](https://doi.org/10.1117/12.671760)
- Fujita, Y., Kawakatu, N., Shlosman, I., & Ito, H. 2016, *MNRAS*, 455, 2289, doi: [10.1093/mnras/stv2481](https://doi.org/10.1093/mnras/stv2481)
- Fujita, Y., & Nagai, H. 2017, *MNRAS*, 465, L94, doi: [10.1093/mnrasl/slw217](https://doi.org/10.1093/mnrasl/slw217)
- Giovannini, G., Cotton, W. D., Feretti, L., Lara, L., & Venturi, T. 2001, *ApJ*, 552, 508, doi: [10.1086/320581](https://doi.org/10.1086/320581)
- Giovannini, G., Savolainen, T., Orienti, M., et al. 2018, *Nature Astronomy*, 2, 472, doi: [10.1038/s41550-018-0431-2](https://doi.org/10.1038/s41550-018-0431-2)
- Giroletti, M., Giovannini, G., Taylor, G. B., et al. 2003, *A&A*, 399, 889, doi: [10.1051/0004-6361:20021821](https://doi.org/10.1051/0004-6361:20021821)
- Giroletti, M., & Polatidis, A. 2009, *Astronomische Nachrichten*, 330, 193, doi: [10.1002/asna.200811154](https://doi.org/10.1002/asna.200811154)
- Goldoni, P., Pita, S., Boisson, C., et al. 2016, *A&A*, 586, L2, doi: [10.1051/0004-6361/201527582](https://doi.org/10.1051/0004-6361/201527582)
- Greisen, E. W. 2003, in *Astrophysics and Space Science Library* 285, *Information Handling in Astronomy – Historical Vistas*, ed. A. Heck (Dordrecht: Kluwer), 109
- Gugliucci, N. E., Taylor, G. B., Peck, A. B., & Giroletti, M. 2005, *ApJ*, 622, 136, doi: [10.1086/427934](https://doi.org/10.1086/427934)
- Haga, T., Doi, A., Murata, Y., et al. 2015, *ApJ*, 807, 15, doi: [10.1088/0004-637X/807/1/15](https://doi.org/10.1088/0004-637X/807/1/15)
- Hardcastle, M. J., Williams, W. L., Best, P. N., et al. 2019, *A&A*, 622, A12, doi: [10.1051/0004-6361/201833893](https://doi.org/10.1051/0004-6361/201833893)
- Harris, D. E., Cheung, C. C., Biretta, J. A., et al. 2006, *ApJ*, 640, 211, doi: [10.1086/500081](https://doi.org/10.1086/500081)
- Hickox, R. C., & Alexander, D. M. 2018, *ARA&A*, 56, 625, doi: [10.1146/annurev-astro-081817-051803](https://doi.org/10.1146/annurev-astro-081817-051803)
- Homan, D. C., Ojha, R., Wardle, J. F. C., et al. 2002, *ApJ*, 568, 99, doi: [10.1086/338701](https://doi.org/10.1086/338701)
- Hovatta, T., Aller, M. F., Aller, H. D., et al. 2014, *AJ*, 147, 143, doi: [10.1088/0004-6256/147/6/143](https://doi.org/10.1088/0004-6256/147/6/143)
- Huchra, J. P., Macri, L. M., Masters, K. L., et al. 2012, *ApJS*, 199, 26, doi: [10.1088/0067-0049/199/2/26](https://doi.org/10.1088/0067-0049/199/2/26)
- Intema, H. T., Jagannathan, P., Mooley, K. P., & Frail, D. A. 2017, *A&A*, 598, A78, doi: [10.1051/0004-6361/201628536](https://doi.org/10.1051/0004-6361/201628536)
- Joye, W. A., & Mandel, E. 2003, *Astronomical Society of the Pacific Conference Series*, Vol. 295, *New Features of SAOImage DS9*, ed. H. E. Payne, R. I. Jedrzejewski, & R. N. Hook, 489
- Kino, M., & Asano, K. 2011, *MNRAS*, 412, L20, doi: [10.1111/j.1745-3933.2010.00996.x](https://doi.org/10.1111/j.1745-3933.2010.00996.x)
- Kino, M., Ito, H., Kawakatu, N., & Nagai, H. 2009, *MNRAS*, 395, L43, doi: [10.1111/j.1745-3933.2009.00638.x](https://doi.org/10.1111/j.1745-3933.2009.00638.x)
- Kino, M., Ito, H., Wajima, K., et al. 2017, *ApJ*, 843, 82, doi: [10.3847/1538-4357/aa7336](https://doi.org/10.3847/1538-4357/aa7336)
- Kino, M., & Kawakatu, N. 2005, *MNRAS*, 364, 659, doi: [10.1111/j.1365-2966.2005.09580.x](https://doi.org/10.1111/j.1365-2966.2005.09580.x)
- Kino, M., Kawakatu, N., & Ito, H. 2007, *MNRAS*, 376, 1630, doi: [10.1111/j.1365-2966.2007.11354.x](https://doi.org/10.1111/j.1365-2966.2007.11354.x)
- Komatsu, E., Dunkley, J., Nolte, M. R., et al. 2009, *ApJS*, 180, 330, doi: [10.1088/0067-0049/180/2/330](https://doi.org/10.1088/0067-0049/180/2/330)

- Kovalev, Y. Y. 2009, *ApJL*, 707, L56, doi: [10.1088/0004-637X/707/1/L56](https://doi.org/10.1088/0004-637X/707/1/L56)
- Kovalev, Y. Y., Petrov, L., Fomalont, E. B., & Gordon, D. 2007, *AJ*, 133, 1236, doi: [10.1086/511157](https://doi.org/10.1086/511157)
- Kovalev, Y. Y., Pushkarev, A. B., Nokhrina, E. E., et al. 2020, *MNRAS*, 495, 3576, doi: [10.1093/mnras/staa1121](https://doi.org/10.1093/mnras/staa1121)
- Kovalev, Y. Y., Aller, H. D., Aller, M. F., et al. 2009, *ApJL*, 696, L17, doi: [10.1088/0004-637X/696/1/L17](https://doi.org/10.1088/0004-637X/696/1/L17)
- Kraft, R. P., Kregenow, J. M., Forman, W. R., Jones, C., & Murray, S. S. 2001, *ApJ*, 560, 675, doi: [10.1086/323056](https://doi.org/10.1086/323056)
- Kraft, R. P., Forman, W., Jones, C., et al. 2000, *ApJL*, 531, L9, doi: [10.1086/312519](https://doi.org/10.1086/312519)
- Krauß, F., Kreter, M., Müller, C., et al. 2018, *A&A*, 610, L8, doi: [10.1051/0004-6361/201732338](https://doi.org/10.1051/0004-6361/201732338)
- Lacy, M., Baum, S. A., Chandler, C. J., et al. 2020, *PASP*, 132, 035001, doi: [10.1088/1538-3873/ab63eb](https://doi.org/10.1088/1538-3873/ab63eb)
- Laurent-Muehleisen, S. A., Kollgaard, R. I., Ryan, P. J., et al. 1997, *A&AS*, 122, doi: [10.1051/aas:1997331](https://doi.org/10.1051/aas:1997331)
- Lewis, J. P. 1995, *Vision Interface*, 120
- Lister, M. L., Aller, M. F., Aller, H. D., et al. 2018, *ApJS*, 234, 12, doi: [10.3847/1538-4365/aa9c44](https://doi.org/10.3847/1538-4365/aa9c44)
- Lister, M. L., Homan, D. C., Kadler, M., et al. 2009a, *ApJL*, 696, L22, doi: [10.1088/0004-637X/696/1/L22](https://doi.org/10.1088/0004-637X/696/1/L22)
- Lister, M. L., Aller, H. D., Aller, M. F., et al. 2009b, *AJ*, 137, 3718, doi: [10.1088/0004-6256/137/3/3718](https://doi.org/10.1088/0004-6256/137/3/3718)
- Lister, M. L., Cohen, M. H., Homan, D. C., et al. 2009c, *AJ*, 138, 1874, doi: [10.1088/0004-6256/138/6/1874](https://doi.org/10.1088/0004-6256/138/6/1874)
- Lister, M. L., Aller, M., Aller, H., et al. 2011, *ApJ*, 742, 27, doi: [10.1088/0004-637X/742/1/27](https://doi.org/10.1088/0004-637X/742/1/27)
- Lister, M. L., Homan, D. C., Hovatta, T., et al. 2019, arXiv:1902.09591. <http://ascl.net/1902.09591>
- Maccagni, F. M., Morganti, R., Oosterloo, T. A., Oonk, J. B. R., & Emonts, B. H. C. 2018, *A&A*, 614, A42, doi: [10.1051/0004-6361/201732269](https://doi.org/10.1051/0004-6361/201732269)
- Marshall, H. L., Miller, B. P., Davis, D. S., et al. 2002, *ApJ*, 564, 683, doi: [10.1086/324396](https://doi.org/10.1086/324396)
- Massaro, F., D'Abrusco, R., Tosti, G., et al. 2012, *ApJ*, 750, 138, doi: [10.1088/0004-637X/750/2/138](https://doi.org/10.1088/0004-637X/750/2/138)
- McConville, W., Ostorero, L., Moderski, R., et al. 2011, *ApJ*, 738, 148, doi: [10.1088/0004-637X/738/2/148](https://doi.org/10.1088/0004-637X/738/2/148)
- Meisenheimer, K., Roser, H. J., Hiltner, P. R., et al. 1989, *A&A*, 219, 63
- Migliori, G., Siemiginowska, A., Kelly, B. C., et al. 2014, *ApJ*, 780, 165, doi: [10.1088/0004-637X/780/2/165](https://doi.org/10.1088/0004-637X/780/2/165)
- Migliori, G., Siemiginowska, A., Sobolewska, M., et al. 2016, *ApJL*, 821, L31, doi: [10.3847/2041-8205/821/2/L31](https://doi.org/10.3847/2041-8205/821/2/L31)
- Müller, C., Kadler, M., Ojha, R., et al. 2014, *A&A*, 562, A4, doi: [10.1051/0004-6361/201322827](https://doi.org/10.1051/0004-6361/201322827)
- Müller, C., Burd, P. R., Schulz, R., et al. 2016, *A&A*, 593, L19, doi: [10.1051/0004-6361/201629547](https://doi.org/10.1051/0004-6361/201629547)
- Nagai, H., Haga, T., Giovannini, G., et al. 2014, *ApJ*, 785, 53, doi: [10.1088/0004-637X/785/1/53](https://doi.org/10.1088/0004-637X/785/1/53)
- Nagar, N. M., Falcke, H., & Wilson, A. S. 2005, *A&A*, 435, 521, doi: [10.1051/0004-6361:20042277](https://doi.org/10.1051/0004-6361:20042277)
- Nelder, J. A., & Mead, R. 1965, *The Computer Journal*, 7, 308, doi: [10.1093/comjnl/7.4.308](https://doi.org/10.1093/comjnl/7.4.308)
- O'Dea, C. P. 1998, *PASP*, 110, 493, doi: [10.1086/316162](https://doi.org/10.1086/316162)
- O'Dea, C. P., & Baum, S. A. 1997, *AJ*, 113, 148, doi: [10.1086/118241](https://doi.org/10.1086/118241)
- Orienti, M., & Dallacasa, D. 2008, *A&A*, 487, 885, doi: [10.1051/0004-6361:200809948](https://doi.org/10.1051/0004-6361:200809948)
- . 2012, *MNRAS*, 424, 532, doi: [10.1111/j.1365-2966.2012.21226.x](https://doi.org/10.1111/j.1365-2966.2012.21226.x)
- Orienti, M., Dallacasa, D., Tinti, S., & Stanghellini, C. 2006, *A&A*, 450, 959, doi: [10.1051/0004-6361:20054656](https://doi.org/10.1051/0004-6361:20054656)
- Ostorero, L., Morganti, R., Diaferio, A., et al. 2017, *ApJ*, 849, 34, doi: [10.3847/1538-4357/aa8ef6](https://doi.org/10.3847/1538-4357/aa8ef6)
- Ostorero, L., Moderski, R., Stawarz, L., et al. 2010, *ApJ*, 715, 1071, doi: [10.1088/0004-637X/715/2/1071](https://doi.org/10.1088/0004-637X/715/2/1071)
- Owsianik, I., Conway, J. E., & Polatidis, A. G. 1998, *A&A*, 336, L37. <https://arxiv.org/abs/astro-ph/9806388>
- Pacholczyk, A. G. 1970, *Radio astrophysics. Nonthermal processes in galactic and extragalactic sources*
- Pashchenko, I. N., & Plavin, A. V. 2019, *MNRAS*, 488, 939, doi: [10.1093/mnras/stz1677](https://doi.org/10.1093/mnras/stz1677)
- Petrov, L., Kovalev, Y. Y., Fomalont, E. B., & Gordon, D. 2008, *AJ*, 136, 580, doi: [10.1088/0004-6256/136/2/580](https://doi.org/10.1088/0004-6256/136/2/580)
- Pihlström, Y. M., Conway, J. E., & Vermeulen, R. C. 2003, *A&A*, 404, 871, doi: [10.1051/0004-6361:20030469](https://doi.org/10.1051/0004-6361:20030469)
- Plavin, A. V., Kovalev, Y. Y., Pushkarev, A. B., & Lobanov, A. P. 2019, *MNRAS*, 485, 1822, doi: [10.1093/mnras/stz504](https://doi.org/10.1093/mnras/stz504)
- Polatidis, A. G. 2009, *Astronomische Nachrichten*, 330, 149, doi: [10.1002/asna.200811143](https://doi.org/10.1002/asna.200811143)
- Principe, G., Migliori, G., Johnson, T. J., et al. 2020, *A&A*, 635, A185, doi: [10.1051/0004-6361/201937049](https://doi.org/10.1051/0004-6361/201937049)
- Protassov, R., van Dyk, D. A., Connors, A., Kashyap, V. L., & Siemiginowska, A. 2002, *ApJ*, 571, 545, doi: [10.1086/339856](https://doi.org/10.1086/339856)
- Pushkarev, A. B., Hovatta, T., Kovalev, Y. Y., et al. 2012, *A&A*, 545, A113, doi: [10.1051/0004-6361/201219173](https://doi.org/10.1051/0004-6361/201219173)
- Refsdal, B. L., Doe, S. M., Nguyen, D. T., et al. 2009, in *Proceedings of the 8th Python in Science Conference*, 51
- Reynolds, C. S., & Begelman, M. C. 1997, *ApJL*, 487, L135, doi: [10.1086/310894](https://doi.org/10.1086/310894)
- Richards, J. L., Max-Moerbeck, W., Pavlidou, V., et al. 2011, *ApJS*, 194, 29, doi: [10.1088/0067-0049/194/2/29](https://doi.org/10.1088/0067-0049/194/2/29)
- Rieger, F. M. 2016, ArXiv 1611.02986. <https://arxiv.org/abs/1611.02986>

- Ryle, Martin, S., & Longair, M. S. 1967, *MNRAS*, 136, 123, doi: [10.1093/mnras/136.2.123](https://doi.org/10.1093/mnras/136.2.123)
- Savolainen, T., Homan, D. C., Hovatta, T., et al. 2010, *A&A*, 512, A24, doi: [10.1051/0004-6361/200913740](https://doi.org/10.1051/0004-6361/200913740)
- Scheck, L., Aloy, M. A., Martí, J. M., Gómez, J. L., & Müller, E. 2002, *MNRAS*, 331, 615, doi: [10.1046/j.1365-8711.2002.05210.x](https://doi.org/10.1046/j.1365-8711.2002.05210.x)
- Shepherd, M. C. 1997, in *Astronomical Society of the Pacific Conference Series*, Vol. 125, *Astronomical Data Analysis Software and Systems VI*, ed. G. Hunt & H. E. Payne (San Francisco: ASP), 77
- Siemiginowska, A., Sobolewska, M., Migliori, G., et al. 2016, *ApJ*, 823, 57, doi: [10.3847/0004-637X/823/1/57](https://doi.org/10.3847/0004-637X/823/1/57)
- Sobolewska, M., Siemiginowska, A., Guainazzi, M., et al. 2019, *ApJ*, 871, 71, doi: [10.3847/1538-4357/aace78](https://doi.org/10.3847/1538-4357/aace78)
- Sokolovsky, K. V., Kovalev, Y. Y., Pushkarev, A. B., & Lobanov, A. P. 2011, *A&A*, 532, A38, doi: [10.1051/0004-6361/201016072](https://doi.org/10.1051/0004-6361/201016072)
- Stanghellini, C., Dallacasa, D., O’Dea, C. P., et al. 2001, *A&A*, 377, 377, doi: [10.1051/0004-6361:20011101](https://doi.org/10.1051/0004-6361:20011101)
- Stark, A. A., Gammie, C. F., Wilson, R. W., et al. 1992, *ApJS*, 79, 77, doi: [10.1086/191645](https://doi.org/10.1086/191645)
- Stawarz, L., Ostorero, L., Begelman, M. C., et al. 2008, *ApJ*, 680, 911, doi: [10.1086/587781](https://doi.org/10.1086/587781)
- Struve, C., & Conway, J. E. 2012, *A&A*, 546, A22, doi: [10.1051/0004-6361/201218768](https://doi.org/10.1051/0004-6361/201218768)
- Taylor, G. B., Wrobel, J. M., & Vermeulen, R. C. 1998, *ApJ*, 498, 619, doi: [10.1086/305586](https://doi.org/10.1086/305586)
- The Fermi-LAT collaboration. 2019, arXiv e-prints, arXiv:1905.10771. <https://arxiv.org/abs/1905.10771>
- Tingay, S. J., Reynolds, J. E., Tzioumis, A. K., et al. 2002, *ApJS*, 141, 311, doi: [10.1086/340783](https://doi.org/10.1086/340783)
- Tingay, S. J., Macquart, J. P., Collier, J. D., et al. 2015, *AJ*, 149, 74, doi: [10.1088/0004-6256/149/2/74](https://doi.org/10.1088/0004-6256/149/2/74)
- Torniainen, I., Tornikoski, M., Turunen, M., et al. 2008, *A&A*, 482, 483, doi: [10.1051/0004-6361:20079222](https://doi.org/10.1051/0004-6361:20079222)
- Tremblay, S. E., Taylor, G. B., Ortiz, A. A., et al. 2016, *MNRAS*, 459, 820, doi: [10.1093/mnras/stw592](https://doi.org/10.1093/mnras/stw592)
- Urry, C. M., & Padovani, P. 1995, *PASP*, 107, 803
- Verkhodanov, O. V., Trushkin, S. A., Andernach, H., & Chernenkov, V. N. 2005, *Bulletin of the Special Astrophysics Observatory*, 58, 118. <https://arxiv.org/abs/0705.2959>
- Voitsik, P. A., Pushkarev, A. B., Kovalev, Y. Y., et al. 2018, *Astronomy Reports*, 62, 787, doi: [10.1134/S1063772918110094](https://doi.org/10.1134/S1063772918110094)
- Weisskopf, M. C., Brinkman, B., Canizares, C., et al. 2002, *PASP*, 114, 1, doi: [10.1086/338108](https://doi.org/10.1086/338108)
- Wilkinson, P. N., Polatidis, A. G., Readhead, A. C. S., Xu, W., & Pearson, T. J. 1994, *ApJL*, 432, L87, doi: [10.1086/187518](https://doi.org/10.1086/187518)
- Willott, C. J., Rawlings, S., Blundell, K. M., & Lacy, M. 1999, *MNRAS*, 309, 1017, doi: [10.1046/j.1365-8711.1999.02907.x](https://doi.org/10.1046/j.1365-8711.1999.02907.x)
- Wójtowicz, A., Stawarz, L., Cheung, C. C., et al. 2020, *ApJ*, 892, 116, doi: [10.3847/1538-4357/ab7930](https://doi.org/10.3847/1538-4357/ab7930)
- Zovaro, H. R. M., Sharp, R., Nesvadba, N. P. H., et al. 2019, *MNRAS*, 484, 3393, doi: [10.1093/mnras/stz233](https://doi.org/10.1093/mnras/stz233)